Nanoparticle Stochastic Impacts at Hard & Soft Interfaces, Supported in an Ionic Liquid

By

Nazanin Ahmadinasab

A thesis submitted to the School of Graduate Studies in partial fulfillment of the requirement for the degree of

Master of Science

Department of Chemistry │ Faculty of Science

Memorial University of Newfoundland

St. John's, NL

April 2022

Abstract

Over the past 20 years, nanoparticle (NP) investigations by single entity electrochemistry (SEE) have become increasingly popular owing to simultaneous acquisition of both catalytic and dynamic NP information. Typically, NPs travel through solution under Brownian motion. When metal NPs randomly collide with an ultramicroelectrode (UME) they can usually be detected through either of two charge transfer processes: (i) complete oxidation of the NP or (ii) electrocatalytic amplification (ECA). In the latter, the metal NP acts as a catalytic surface lowering the driving force of reaction (*i.e.*, necessary applied potential), greatly enhancing the measured current signal. Owing to their random motion, NPs impact the surface and then move way or are consumed which generates a 'current spike' with a characteristic profile in the recorded chronoamperogram (*i-t* curve). Herein, Pt and $LiBH_4$ nanocrystals (NCs) prepared in trihexyltetradecylphosphonium bis(trifluoromethylsulphonyl)imide ($P_{66614}NTf_2$), an ionic liquid (IL), were studied at both solid/IL (UME) and soft (water|IL) micro-interfaces. Pt NPs showed electrocatalytic activity for borohydride oxidation reaction (BOR) and methanol oxidation reaction (MOR) through ECA. Also, this method was used for calculating the size of $LiBH_4$ dielectric nanocrystals (NCs) by integrating the *i-t* curve beneath the current spikes, which compared favourably to NP sizes determined from TEM micrographs.

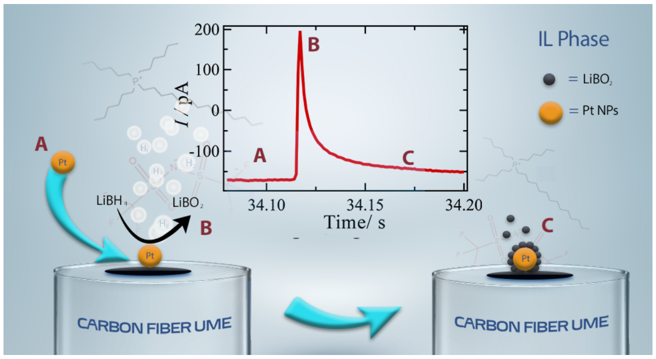

Acknowledgements

First, I would like to express my deepest appreciation to my supervisor Dr. Talia J. Stockmann for her kind support and advice. This work would have not been possible without her valuable academic knowledge and guidance. I'm extremely grateful to my co-supervisor Dr. Peter G. Pickup for his consideration.

My heartfelt thanks to my committee members Dr. Graham J. Bodwell and Dr. Yuming Zhao for their useful feedback. Also, specially thanks to School of Graduate Studies for their financial support.

I am deeply indebted to my family, specially my husband for their patient and emotional support. Also, I would like to extend my gratitude to my friends and colleagues Abhishek, Reza, Qi, Mona, and Siamak.

Specially thanks to university staff Debbie, Mary, and Stephanie Tucker for their help during my Master's degree.

Contents

List of Figures

List of Tables

List of Abbreviations

Abbreviation	**Description**
BMIM	1-Butyl-3-methylimizolium
BOR	Borohydride oxidation reaction
CA	Chronoamperometry
CF	Carbon fiber
CV	Cyclic voltammetry
DCB	1,2-Dichlorobenzene
DCE	1,2-Dichloroethane
DLS	Dynamic light scattering
DNA	Deoxyribonucleic acid
ECA	Electrocatalytically amplified
E_{PZC}	Effective point of zero charge
ET	Electron transfer
FIT	Facilitated ion transfer
GC	Glassy carbon
GCE	Glassy carbon electrode
GNPs	Graphene NPs
IL	Ionic liquid
IT	Ion transfer
ITIES	Interface between two immiscible electrolyte solutions
MOR	Methanol oxidation reaction

NC	Nanocrystal
NIE	Nano-impact electrochemistry
NMR	Nuclear magnetic resonance
NP	Nanoparticle
ORR	Oxygen reduction reaction
PPW	Polarized potential window
RTIL	Room temperature ionic liquid
SEE	Single entity electrochemistry
SEM	Scanning electron microscopy
SLEI	Solid liquid electrochemistry interface
TEM	Transmission electron microscopy
UME	Ultramicroelectrode

List of Symbols

A	Ampere
μm	Micrometer
$\mu_{\alpha,i}$	Electrochemical potential of species *i* in phase α
A	Electrode surface
$a_{\alpha,i}$	Activity of ion *i* in phase α
C	Concentration
c_j^*	Bulk concentration of species j
D_{NP}	Diffusion coefficient
E	Potential
F	Faraday constant
f	Frequency
i	Current
i_{ss}	Steady state current
L	Litre(s)
mM	Millimolar
M_w	Molecular weight
n	Number of electrons transferred
nA	Nanoampere
Q	Charge transferred
R	Universal gas constant

r_{NP}	Radius of nanoparticle
s	Second
t	Time
T	Temperature in degrees Kelvin
v	Scan rate
V	Voltage
w|IL	Water|Ionic liquid
Z_i	Charge of species *i*
ΔG	Standard Gibbs energy
$\Delta G^{\circ}_{\mathrm{i.tr\ w\rightarrow o}}$	Gibbs energy of ion transfer of *i* from water to the organic phase
ρ	Density
ϕ_{α}, ϕ_{β}	Inner potential of α and β phases
∇^2	the Laplacian operator presented in cylindrical coordinates

Chapter 1

State-of-the-art in electrochemical stochastic impacts

1.1. Single Entity Detection

Single entity detection is defined as the act of studying one entity at a time;[1] where an 'entity' typically means a single molecule, nanoparticle, live cell, etc. Unlike ensemble measurements, observing small quantities of a system individually can provide better understanding of rare subpopulations, hidden intermediates, and unique reaction pathways/dynamics. In ensemble methods, like dynamic light scattering (DLS), large entities usually overshadow the existence and reactivity of smaller ones and important systemic information can be lost.[2]

Indeed, with recent technological advancements, this emerging field has grown to include single entity electrochemistry (SEE) techniques that push the lower end of the detection limit from the micron to the nanoscale in terms of object size. This is a promising area of research which exploits non-faradaic and faradaic processes for ion or charge transfer to obtain physical insight into how single entities behave. Resistive pulse sensing, whose earliest incarnation was the Coulter Counter method, is one of the pioneering examples, and nano-impact electrochemistry (NIE) is a recent example of SEE.[1] In fact, when applied to metal and dielectric nanoparticles (NPs) these methods can provide information about size, charge, and catalytic properties. Two dominant SEE methods are reviewed below along with ionic liquids, ionic solvents which provide a novel media for SEE analysis, and liquid|liquid interfacial electrochemistry, a recent platform for a host of SEE detection methods. The latter has only recently been applied to SEE investigations and has revealed fascinating new mechanistic and kinetic insights into nanoparticle interactions.

1.1.1. Resistive-pulse sensing

Resistive-pulse sensing is defined as a SEE technique for counting and sizing particles in an ionic solution. The earliest form of resistive-pulse sensing was the Coulter Counter method developed by Wallace H. Coulter.[3] The Coulter principle is based on ionic current flowing through a pore positioned between two chambers containing electrolyte solutions. As an object (bacteria or live cell) passes through the pore, the ionic current is disrupted and can be measured.[4] The degree to which the current is blocked or enhanced (Δi) is proportional to the size of the object occluding the orifice and was originally used to count bacteria and live cells in solution. It has recently been adapted for smaller and smaller objects such as in the study of NPs and biomolecules (see Figure 1.1). For example, in 1996, Kasianowicz *et al*.[5] revealed the first experiment in Coulter Counter-based resistive-pulse sensing with the demonstration of single-stranded DNA detection using a biological α-hemolysin pore.

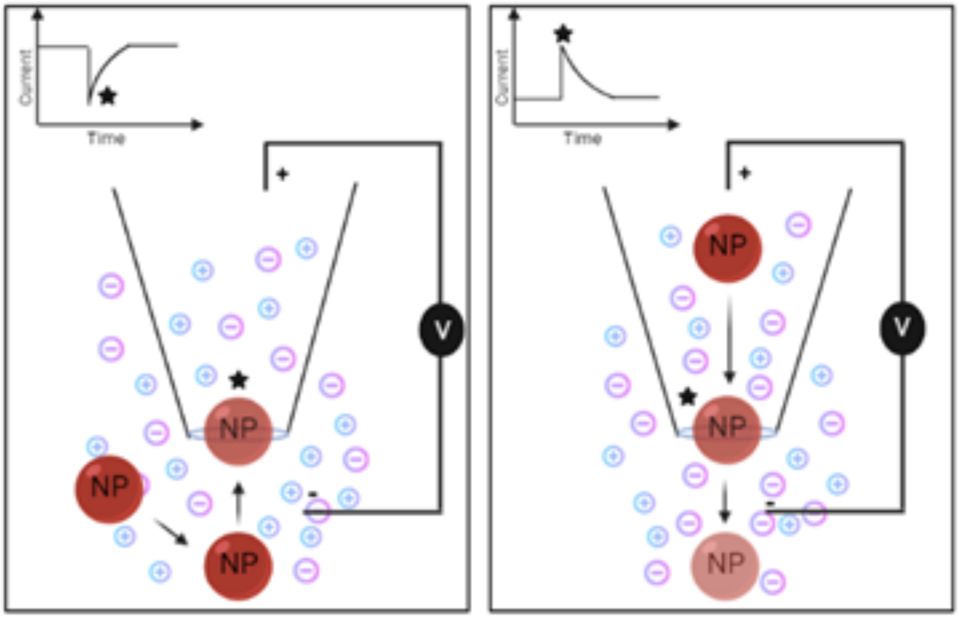

Figure 1.1: Cartoon of a nanoparticle (NP) blocking a pore eliciting a resistive pulse in the ionic current signal.

In this method, increasing the speed of particle's translocation could decrease the measurement sensitivity.[6] For example, in nanopore-based DNA sequencing methods, the voltage is applied across the pore to drive the DNA molecules to enter the pore. When DNA passes through the nanopore, the ionic current decreases similar to resistive pulse sensing/the Coulter Counter method discussed above. By monitoring this current change, a specific DNA sequence can be obtained. Controlling the speed of DNA translocation through the pore is very challenging and often occurs too quickly for contemporary instrumentation to discriminate between individual base-pairs.[7] The speed of DNA translocation depends on the viscosity of the solution.

Since most of the ILs have high viscosity, the translocation speed in IL would be slower than in other solvents. Because of that, in the past decade, ILs have been investigated for DNA sequencing applications. For example, Kulkarni *et al.*[8] in 2016 studied the effect of 1-butyl-3-methylimizolium chloride (BMIM-Cl) IL on hetero-nucleotide sequence $d(ACGT)_5$ translocation speed through a graphene nanopore compared with KCl as a conventional electrolyte. As a result, the distribution of $BMIM^+$ was much higher than K^+ near the nanopore. Therefore, the electrostatic interaction between $BMIM^+$ and the negative charge of $d(ACGT)_5$ could reduce the speed of DNA translocating through the nanopore. Also, they suggested that the speed of DNA translocation would be reduced by using a solid-state nanopore and viscose IL.

J. Feng *et al.*[9] solved the problem of DNA translocation across two-dimensional materials like molybdenum disulphide (MoS_2) by using an IL. An interesting outcome of their work was that by dissolving the **λ**-dsDNA in $BMIM\text{-}PF_6$ in the cis-chamber (where DNA is initially placed) and KCl in water in the trans-chamber (where DNA translocates to) after applying the potential, the motion of DNA became 10-50 times slower across the 2.8 nm MoS_2 pore. They found that an increase in the noise during translocation may be due to electrostatic interaction between the cationic $BMIM^+$ and DNA phosphates.

1.1.2. Nano-Impact Method

The nano-impact method is a novel electrochemical technique used to study single NP stochastic collisions at an electrode surface, typically employing an ultramicroelectrode (UME), *i.e.*, an inlaid disc electrode with a diameter of <25 μm. This method is based on the Brownian motion of NPs. This means that NPs in solution randomly collide with the electrode surface. The results of these collisions can be recorded electrochemically by chronoamperometry (CA) as current ‘spikes’. The change in current is brought about through one of a handful of different electrochemical processes, including capacitive, blocking, direct faradaic, and mediated faradaic.[10]

Each electrochemical possibility is described in the following sections. However, from NP impacts, the size, concentration, degree of aggregation, and catalytic reactivity can often be obtained. Moreover, this method can provide a useful way to study electrocatalysis at single metal NPs.

1.1.2.1. Direct Faradaic Collision

In this mechanism, the particle is oxidized or reduced at the electrode and during this redox reaction electrons transfer between the particle to the electrode. If one assumes complete oxidation/reduction of the particle, then the size of the particle can be calculated as a function of the amount of charge transferred since,

$$\begin{aligned} i &= \frac{dQ}{dt} \\ dQ &= idt \\ Q &= \int idt \end{aligned} \tag{1.1}$$

Then the total charge transferred (Q) can be determined. Next, by assuming that the particle geometry is perfectly spherical, the radius of the particle (r_{NP}) can be obtained from the following equation,[10-12]

$$Q = \frac{\frac{4}{3}\pi r_{\mathrm{NP}}^{3} n \rho F}{M_w} \tag{1.2}$$

where ρ, n, M_w, and F are the density, number of electrons transferred, molecular weight of the material composing the NP, and Faraday’s constant, respectively.

For example, Tanner *et al.*[13] in 2016 studied the effect of chloride ion on the direct oxidation of silver NPs in 1-butyl-3-methylimizolium tetrafluoroborate ([BMIM][BF_4]) through the nano-impact method. They accelerate Ag oxidation by adding Cl^- and compared the electrochemical sizing of Ag NPs with the SEM method and found excellent agreement between the two methods. This is a critical finding as electrochemical methods are easier and cheaper to employ, while SEM techniques require specialized training, sampling methods, and high cost of operation. A similar study was also performed using Au NPs, in 2012.[14] They determined the Au NP impacts at a glassy carbon electrode (GCE) with an anodic particle coulometry method in the presence of acidic solvents. By measuring the current transient of Au NP oxidation impacts at a GCE and from cyclic voltammetric (CV) records, they found that $\mathrm{AuCl_2^-}$ and $\mathrm{AuCl_4^-}$ complexes were the main contributors to the oxidative transient. Therefore, this method was not only used for detecting the size and number of NPs but was also used to study the mechanism of NP oxidation.

1.1.2.2. Meditated Faradaic Impacts

Meditated faradaic impacts, also known as electrocatalytically amplified (ECA) impacts, are when the particle acts as an electrocatalyst; however, unlike the direct faradaic collision, they are not consumed during the reaction. This can result in 10× or 20× current enhancement as the NP collides with the UME surface.

For example, Xiao *et al.*[15] in 2007 used the ECA method for observing electrochemically the collisions of Pt NPs at a carbon fiber (CF) UME. Pt NPs electrocatalyzed the reduction of protons to $H_2(g)$. The diagram in Figure 1.2 shows the characteristic movement and associated signal as NPs in solution (A) collide with the electrode surface (B), then act as electrocatalysts mediating a redox reaction which generates a sudden current increase. Then, as they diffuse away from the electrode surface (C), this results in an exponential decay in the *i-t* profile. In this way, information can be gained about the dynamics and kinetics of the process at the single-particle level.

Although ECA is a powerful method to study the electrocatalytic behaviors of NP, it is also used to detect other aspects of electrochemical properties of NPs. For example, Fernando *et al.*[16] in 2013 expanded the ECA method to the detection of TiO_2 NPs by exploiting the photoelectrochemical properties of anatase. They considered photooxidation of MeOH by TiO_2 NPs at Pt UME to observe the photogenerated electron mechanism.

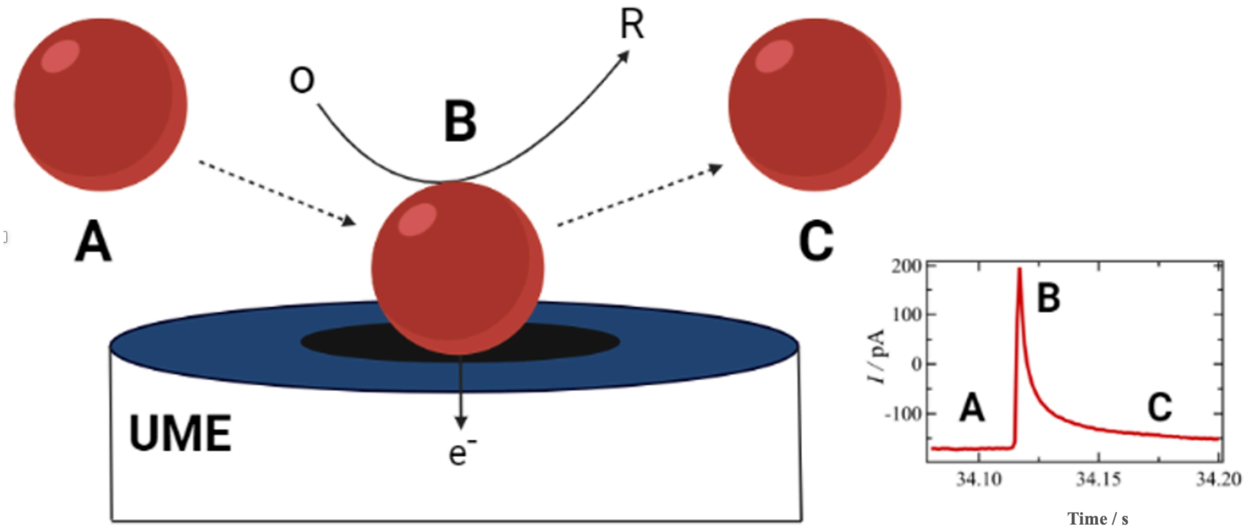

Figure 1.2: Schematic of the effect of electrocatalytically amplified impact events. NPs travel through the solution **(A)** and randomly collide with the electrode surface **(B)**. They act as electrocatalysts for redox reactions and leave the surface **(C)**.

1.1.2.3. Capacitive Impact

In the case of capacitive impacts, the electron transfers through two ways: electrolyte interface and particle impact's charging. In both, there is no redox reaction; however, the charge distribution at the interface is changed and is in essence a non-faradaic process. If a NP is absorbed at a liquid|liquid interface, it disrupts the back-to-back double electric layers.[17] For example, Stockmann *et al.*[18] studied $LiBH_4$ nanocrystal (NC) stochastic impacts at a water|ionic liquid micro-interface. They proposed that NCs absorbed at the interface and generated the capacitive response either through H_2 bubble formation via hydrolysis of $LiBH_4$ or directly through NC adsorption. Also, Poon *et al.*[19] by using the nano-impact method, studied graphene NPs (GNPs) at cylindrical carbon fiber wire and they observed spikes in the *i-t* curves in response to capacitive impact of GNPs. From the GNPs impacts, they determined the potential of zero charge and diffusion coefficient of GNPs.

1.1.2.4. Blocking Impact

In the blocking impacts mechanism, the particle collides and binds to the electrode surface inhibiting any redox processes from taking place. In this way, these types of NPs are non-conductive/non-reactive and essentially shield or deactivate the electrode surface. If redox reactions are taking place at the UME, blocking particles will inhibit this process and decrease the observed current until the particle is consumed or leaves the electrode.

In 2004, Lemay *et al.*[20] used ferrocene methanol ($FcCH_2OH$) as a redox mediator at a Au UME in the presence of carboxylated latex beads. By biasing the potential above $FcCH_2OH$'s oxidation potential a steady state current was generated. As polymer beads adsorbed onto the Au UME surface, its reactive surface area was slowly decreased and periodic drops in the observed *i-t* profile, or current steps were recorded. Beads effectively blocked mass transport of $FcCH_2OH$ to the surface.

1.2. Ionic Liquid

Ionic liquids (IL) are defined as salts with melting points below 100°C and are typically composed of large organic cations and anions. Exact estimation of when IL was discovered is impossible because the definition of what is an IL has been changed over the years. In many sources in the literature,[21-22] the first IL was thought to have been synthesized in 1927. During the Friedel–Crafts reactions, an organic liquid salt was synthesized and comprised of a carbocation with tetracholoroaluminate anions.

1.2.1.1. Properties of ILs

IL properties are tied to their structure and the pairing of different anions and cations together.[23] Long-range Coulombic interactions combined with hydrophobic, van der Waals, and other intermolecular interactions provide a holistic view of IL fluidic properties. Most ILs exhibit high viscosity and a low melting point;[24] however, they also have high thermal stability, high electrical conductivity, and low vapor pressure, all of which are strongly dependent on their anion and cation. For example, Pringle *et al.*,[25] in 2013, studied the physical properties of a room temperature IL (RTIL) with bis(trifluoromethanesulfonyl)imide (NTf_2^-) as a fluorinated anion. As a result, they found that fluorinated anions increase viscosity, as well as thermal and electrochemical stability of RTIL.

Besides, some anions are commonly cited as a reason for hydrophobic ILs. In Figure 1.3 a few common anions that produce hydrophobic ILs are shown. These kinds of ILs are famous for use as solvents in dehydration reactions,[26] and moisture- sensitive reactions.

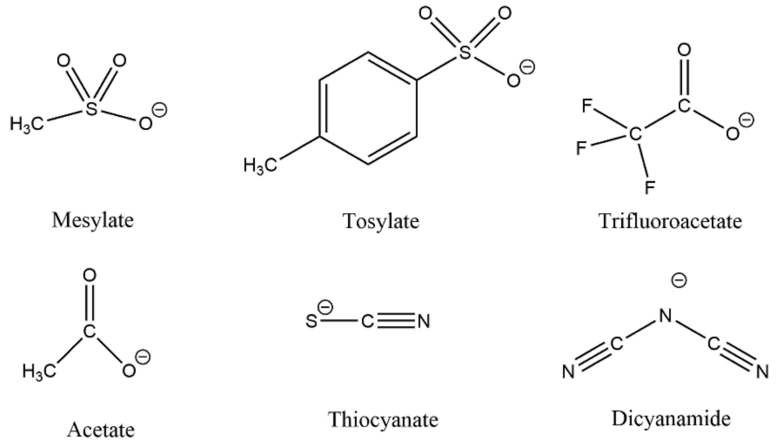

Figure 1.3: Some commons anions producing hydrophobic ionic liquids.

During this research program, the tetraalkylphosphonium-based IL ($P_{66614}NTf_2$) was used because it is hydrophobic but also has a reasonable viscosity at room temperature, while being highly electrochemically stable. Its structure is shown in Figure 1.4.

Stockmann *et al.*[27] in 2012 measured the density, viscosity, and conductivity of both trihexyltetradecylphosphonium tetrakis(pentafluorophenyl)borate ($P_{66614}TB$) and $P_{66614}NTf_2$ and compared these values with those obtained using cyclic voltammetry (CV) and ferrocene/ferrocenium (Fc/Fc^+) redox couple at varying temperatures. The results showed that by increasing the temperature from 25 to 90 °C the viscosity was reduced from 332.3 to 36.3 mPa s for $P_{66614}NTf_2$ and from 179993.8 to 245.7 mPa s for $P_{66614}TB$.

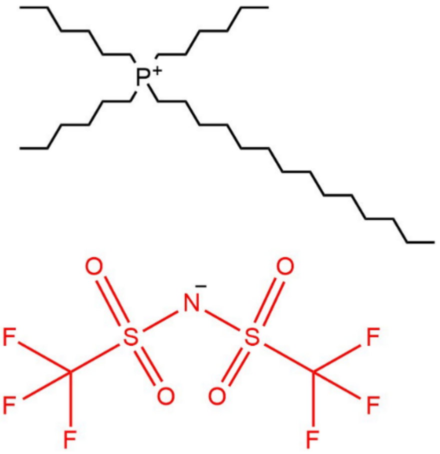

Figure 1.4: Chemical structure of $P_{66614}NTf_2$.

1.2.1.2. Applications of ILs

1.2.1.2.1. ILs for Synthesis the Metal NPs

In the past 20 years, ILs have attracted much attention as solvents for the preparation of metal-NPs for different catalytic reactions. Overall, the low interfacial tension in ILs generates highly monodisperse NPs. The cations and anions that constitute an IL form an electrostatic shell around the NP, preventing NP aggregation.[28] For example, Rossi *et al.*[29] in 2004 synthesized RuO_2 NPs with diameters averaging 2.4±0.5 nm by dissolving $RuCl_3$ in an imidazolium IL [$BMI.PF_6$] and using $NaBH_4$ as a reducing agent. They found that the resulting RuO_2 NPs could act as recyclable solid catalysts to hydrogenate C=C bonds under mid conditions.

Also, Dupont *et al.*[30] used the same IL to synthesize Ir NPs by employing ligand reduction to enhance the biphasic and hydrogenation of various olefines. TEM imaging showed that the Ir NPs were ~2 nm in diameter.

1.2.1.2.2. ILs in Electrochemistry

In addition, some ILs can dissolve both organic and inorganic components. This feature turns ILs into ideal solvents for homogeneous catalysis. [31-32]

Because of their high conductivity, wide thermal stability, and a large window of electrochemical stability, ILs are known as suitable electrolytes for electrochemical applications like rechargeable batteries and energy storage devices.[33] For example, using an IL as the electrolyte in lithium-based batteries increases the cycling stability and decreases flammability. Aluminum-based batteries using aqueous electrolytes suffer from aluminum hydroxide formation on the Al surface, so ILs could be a suitable alternative for the aqueous electrolyte.[34]

1.3. Liquid|Liquid interface *vs.* Solid|Liquid Interface

Many electrochemical techniques employ solid/electrolyte interfaces to study a range of charge transfer processes. This history dates back 150 years, when Helmholtz[35] introduced the double layer phenomena, *i.e.*, the water and supporting electrolyte structure at the solid electrode/electrolyte surface.[36]

Solid electrodes are used in a broad range of electrocatalytic mechanisms. For example, recently, Su *et al.*[37] demonstrated the single Ni atom electrocatalytic mechanism for oxygen reduction reaction using operando synchrotron spectroscopies at solid|liquid interface. Single Ni atoms released from the electrode surface formed isolated-zigzag $\mathrm{Ni}_1^{(2-\delta)+}\mathrm{N}_2$ active site that could catalyze oxygen reduction reaction.

In 1970, Gavach *et al*.[38] showed that the liquid|liquid interface can be polarized as well as the electrode|electrolyte interface. The liquid|liquid interface, also known as an interface between two immiscible electrolyte solutions (ITIES), can be between water|oil (w|o). In the past 20 years, the ITIES has found many applications in extraction processes, chemical sensing, and the detection of ionic species. In contrast to the solid|electrolyte interface, both electron transfer (ET), ion transfer (IT), and facilitated ion transfer (FIT) processes can be studied at the liquid|liquid interface (Figure 1.5).

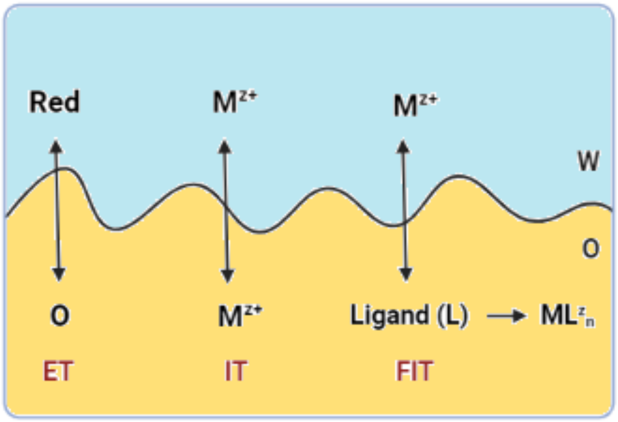

Figure 1.5: Schematic representation of ET, IT, and FIT at liquid|liquid interface. At the ITIES, the electron or ion can be transferred across the liquid|liquid interface (ET and IT). In some cases, the ion, after transferring, forms an ion-complex (FIT).

1.4. Scope of the Thesis

Since NPs play increasingly vital roles in human life, the study of NP behavior is important. SEE is a powerful method to detect and characterize NPs as well as evaluate their dynamic behaviour. The goal of this work was to investigate electrochemical interactions of single Pt NP at both hard and soft interfaces within an IL.

In Chapter 2, the synthesis of tiny and low dispersity Pt NPs in $P_{66614}NTF_2$ IL as solvent and $LiBH_4$ as reducing agent is demonstrated. Also, experiments of 1.2 M $LiBH_4$ dissolved in $P_{66614}NTF_2$ at a CF UME provide evidence of the presence of $LiBH_4$ nanocrystals (NCs). The size of the NCs was determined through the faradaic nano-impact method by assuming that all $LiBH_4$ NCs were completely oxidized at the CF UME surface. In addition, the electrocatalytic behavior of Pt NPs for BH_4 oxidation reaction (BOR) in IL is also described.

In Chapter 3, preliminary investigations of $LiBH_4$ NC and Pt NP impacts at a micro liquid|liquid interface are described. By measuring the current with time for Pt NPs-IL solution in the presence of $LiBH_4$, Pt NP catalytic pathways are proposed for both BH_4^- as well as CH_3OH oxidation.

Finally, Chapter 4 a summary of the results and a perspective of NP investigations in an IL medium at both solid|solution and IL|water interfaces is presented.

1.5. References

1. Baker, L. A., Perspective and Prospectus on Single-entity Electrochemistry. *J. Am. Chem. Soc.* **2018,** *140* (46), 15549-15559.

2. Ying, Y.-L.; Wang, J.; Leach, A. R.; Jiang, Y.; Gao, R.; Xu, C.; Edwards, M. A.; Pendergast, A. D.; Ren, H.; Weatherly, C. K. T., Single-entity Electrochemistry at Confined Sensing Interfaces. *Sci. China Chem.* **2020,** *63* (5), 589-618.

3. Song, Y.; Zhang, J.; Li, D., Microfluidic and Nanofluidic Resistive Pulse Sensing: A Review. *Micromachines* **2017,** *8* (7), 204.

4. Pan, R.; Hu, K.; Jiang, D.; Samuni, U.; Mirkin, M. V., Electrochemical Resistive-pulse Sensing. *J. Am. Chem. Soc.* **2019,** *141* (50), 19555-19559.

5. Kasianowicz, J. J.; Brandin, E.; Branton, D.; Deamer, D. W., Characterization of Individual Polynucleotide Molecules Using A Membrane Channel. *PNAS* **1996,** *93* (24), 13770-13773.

6. Bayley, H.; Martin, C. R., Resistive-pulse Sensing from Microbes to Molecules. *Chem. Rev.* **2000,** *100* (7), 2575-2594.

7. Carson, S.; Wanunu, M., Challenges in DNA Motion Control and Sequence Readout Using Nanopore Devices. *Nanotechnology* **2015,** *26* (7), 074004.

8. Kulkarni, M.; Mukherjee, A., Ionic Liquid Prolongs DNA Translocation Through Graphene Nanopores. *RSC Advances* **2016,** *6* (51), 46019-46029.

9. Feng, J.; Liu, K.; Bulushev, R. D.; Khlybov, S.; Dumcenco, D.; Kis, A.; Radenovic, A., Identification of Single Nucleotides in MoS_2 Nanopores. *Nat. Nanotechnol.* **2015,** *10* (12), 1070-1076.

10. Sokolov, S. V.; Eloul, S.; Kätelhön, E.; Batchelor-McAuley, C.; Compton, R. G., Electrode–particle Impacts: A Users Guide. *Phys. Chem. Chem. Phys.* **2017,** *19* (1), 28-43.

11. Kätelhön, E.; Tanner, E. E.; Batchelor-McAuley, C.; Compton, R. G., Destructive Nano-Impacts: What Information Can Be Extracted from Spike Shapes? *Electrochim. Acta* **2016,** *199*, 297-304.

12. Brasiliense, V.; Patel, A. N.; Martinez-Marrades, A.; Shi, J.; Chen, Y.; Combellas, C.; Tessier, G.; Kanoufi, F., Correlated Electrochemical and Optical Detection Reveals the Chemical Reactivity of Individual Silver Nanoparticles. *J. Am. Chem. Soc.* **2016,** *138* (10), 3478-3483.

13. Tanner, E. E.; Batchelor-McAuley, C.; Compton, R. G., Single Nanoparticle Detection in Ionic Liquids. *J. Phys. Chem. C* **2016,** *120* (3), 1959-1965.

14. Zhou, Y.-G.; Rees, N. V.; Pillay, J.; Tshikhudo, R.; Vilakazi, S.; Compton, R. G., Gold Nanoparticles Show Electroactivity: Counting and Sorting Nanoparticles Upon Impact with Electrodes. *ChemComm.* **2011,** *48* (2), 224-226.

15. Xiao, X.; Bard, A. J., Observing Single Nanoparticle Collisions at an Ultramicroelectrode by Electrocatalytic Amplification. *J. Am. Chem. Soc.* **2007,** *129* (31), 9610-9612.

16. Fernando, A.; Parajuli, S.; Alpuche-Aviles, M. A., Observation of Individual Semiconducting Nanoparticle Collisions by Stochastic Photoelectrochemical Currents. *J. Am. Chem. Soc.* **2013,** *135* (30), 10894-10897.

17. Kakiuchi, T.; Chiba, M.; Sezaki, N.; Nakagawa, M., Cyclic Voltammetry of the Transfer of Anionic Surfactant Across The Liquid–liquid Interface Manifests Electrochemical Instability. *Electrochem. Commun.* **2002,** *4* (9), 701-704.

18. Stockmann, T. J.; Lemineur, J.-F.; Liu, H.; Cometto, C.; Robert, M.; Combellas, C.; Kanoufi, F., Single $LiBH_4$ Nanocrystal Stochastic Impacts at a Micro Water|Ionic Liquid Interface. *Electrochem. Acta* **2019,** *299*, 222-230.

19. Poon, J.; Batchelor-McAuley, C.; Tschulik, K.; Compton, R. G., Single Graphene Nanoplatelets: Capacitance, Potential of Zero Charge and Diffusion Coefficient. *Chem. Sci. J.* **2015,** *6* (5), 2869-2876.

20. Quinn, B. M.; Van't Hof, P. G.; Lemay, S. G., Time-resolved Electrochemical Detection of Discrete Adsorption Events. *J. Am. Chem. Soc.* **2004,** *126* (27), 8360-8361.

21. Forsyth, S. A; Pringle, J. M; MacFarlane, D. R., Ionic Liquids—An Overview. *Aust. J. Chem.* **2004,** *57* (2), 113-119.

22. Wilkes, J. S., A Short History of Ionic Liquids—From Molten Salts to Neoteric Solvents. *Curr. Green Chem.* **2002,** *4* (2), 73-80.

23. Kianfar, E.; Mafi, S., Ionic Liquids: Properties, Application, and Synthesis. *Chem. Eng. J.* **2021**, 22-31.

24. McDaniel, J. G.; Yethiraj, A., Understanding The Properties of Ionic Liquids: Electrostatics, Structure Factors, and Their Sum Rules. *J. Phys. Chem. B* **2019,** *123* (16), 3499-3512.

25. Pringle, J. M.; Golding, J.; Baranyai, K.; Forsyth, C. M.; Deacon, G. B.; Scott, J. L.; MacFarlane, D. R., The Effect of Anion Fluorination in Ionic Liquids—Physical Properties of a Range of Bis(methanesulfonyl) Amide Salts. *New J. Chem.* **2003,** *27* (10), 1504-1510.

26. Shi, F.; Xiong, H.; Gu, Y.; Guo, S.; Deng, Y., The First Non-acid Catalytic Synthesis of tert-Butyl Ether From tert-Butyl Alcohol Using Ionic Liquid as Dehydrator. *Chem. Commun.* **2003,** (9), 1054-1055.

27. Stockmann, T. J.; Zhang, J.; Wren, J. C.; Ding, Z., Hydrophobic Alkylphosphonium Ionic Liquid for Electrochemistry at Ultramicroelectrodes and Micro Liquid| Liquid Interfaces. *Electrochem. Acta* **2012,** *62*, 8-18.

28. Richter, K.; Campbell, P. S.; Baecker, T.; Schimitzek, A.; Yaprak, D.; Mudring, A. V., Ionic Liquids for The Synthesis of Metal Nanoparticles. *Phys. Status Solidi B* **2013,** *250* (6), 1152-1164.

29. Rossi, L. M.; Dupont, J.; Machado, G.; Fichtner, P. F.; Radtke, C.; Baumvol, I. J.; Teixeira, S. R., Ruthenium Dioxide Nanoparticles in Ionic Liquids: Synthesis, Characterization and Catalytic Properties in Hydrogenation of Olefins and Arenes. *J. Braz. Chem. Soc.* **2004,** *15*, 901-910.

30. Dupont, J.; Fonseca, G. S.; Umpierre, A. P.; Fichtner, P. F.; Teixeira, S. R., Transition-Metal Nanoparticles in Imidazolium Ionic Liquids: Recycable Catalysts for Biphasic Hydrogenation Reactions. *J. Am. Chem. Soc.* **2002,** *124* (16), 4228-4229.

31. Ptak, S.; Zarski, A.; Kapusniak, J., The Importance of Ionic Liquids in The Modification of Starch and Processing of Starch-based Materials. *Materials* **2020,** *13* (20), 4479.

32. Wilpiszewska, K.; Spychaj, T., Ionic Liquids: Media for Starch Dissolution, Plasticization and Modification. *Carbohydr. Polym.* **2011,** *86* (2), 424-428.

33. Kim, E.; Han, J.; Ryu, S.; Choi, Y.; Yoo, J., Ionic Liquid Electrolytes for Electrochemical Energy Storage Devices. *Materials* **2021,** *14* (14), 4000.

34. Yang, Q.; Zhang, Z.; Sun, X.-G.; Hu, Y.-S.; Xing, H.; Dai, S., Ionic Liquids and Derived Materials for Lithium and Sodium Batteries. *Chem. Soc. Rev.* **2018,** *47* (6), 2020-2064.

35. Jerkiewicz, G., From Electrochemistry to Molecular-Level Research on the Solid—Liquid Electrochemical Interface: An Overview. **1997**.

36. Delahay, P., Double Layer Studies. *J. Electrochem. Soc.* **1966,** *113* (10), 967.

37. Su, H.; Zhou, W.; Zhang, H.; Zhou, W.; Zhao, X.; Li, Y.; Liu, M.; Cheng, W.; Liu, Q., Dynamic Evolution of Solid–liquid Electrochemical Interfaces Over Single-atom Active Sites. *J. Am. Chem. Soc.* **2020,** *142* (28), 12306-12313.

38. Gavach, C.; Mlodnicka, T.; Guastalla, J., CRH Seances Acad. *Sci. Ser. C* **1968,** *266*, 1196-1199.

Chapter 2

Single entity electrochemical detection of as-prepared metallic and dielectric nanoparticle stochastic impacts in a phosphonium ionic liquid

2.1 Statement of Co-Authorship

This chapter has been submitted under the above title and has been published in the journal N. Ahmadinasab, T. J. Stockmann,* *ChemElectroChem*, **2022**, ahead of print, doi:10.1002/celc.202200162.

NA is the first author as she performed >98% of the experimental work and analyzed the data. TJS designed the experiments, performed computational simulations, wrote the first draft of the manuscript, performed data analysis, acquired funding for the research program, and edited as well as finalized the manuscript.

2.2. Introduction

In its simplest form, and as recently described by Baker,[1] single entity electrochemistry (SEE) is the act of studying/detecting one "entity" at a time using electrochemical means and has become of increasing interest owing to the technological developments in low current instrumentation. "Entities" in this case encompasses a broad range of materials on the molecular, micron, and nanoscale,[1, 2] including metal[3] and inorganic nanoparticles (NPs);[4-8] biomolecules[9-12] and live cells/bacteria;[13-15] vesicles;[16] and single molecules.[17-19] SEE investigations have expanded from the usual solid electrode/electrolyte interface, often performed using a nano or ultramicroelectrode (UME),[20] and now include soft, liquid|liquid interfaces.[4, 5, 21-23]

Metal and dielectric NPs, however, are of interest owing to their unique catalytic[5] and optical[24-27] properties. Movement of metal and dielectric NPs through solution under Brownian motion results in stochastic impacts at the UME surface which are recorded as 'spikes' typically in the current-time (*i-t*) domain, *i.e.*, with chronoamperometry (CA). The change in current can be owing to capacitive, blocking as well as direct or mediated faradaic processes.[2] In the latter two, direct faradaic impacts can lead to the consumption/dissolution of the NP through an oxidative/reductive process,[28] while for mediated faradaic impacts the NP remains unchanged; however, it behaves as a site for electrocatalyzing a heterogeneous reaction. Xiao *et al.*[3] reported one of the first cases of the latter, electrocatalytic amplification (ECA) of Pt NPs impacting a carbon fibre (CF) UME and catalyzing the H_2 evolution reaction (HER). The frequency of NP impacts can also be linked to the concentration of NPs in solution.

Later, Compton's[29] and Kanoufi's[4] groups investigated NP impacts within an ionic liquid phase (IL). ILs are molecularly large organic salts with melting points below 100°C that can enhance catalysis. They are also excellent media for growing small (<20 nm diameter) and low dispersity (<±2-5 nm) NPs[30-32] and have numerous advantageous physicochemical properties, *e.g.*, high thermal and electrical stability, that make them highly desirable, designer solvents.[30] Tanner *et al.*'s study of NP impacts employed a hydrophilic imidazolium based IL with the Ag NPs prepared and modified in an aqueous solution, then transferred to the IL phase.[29] Ag NPs were detected *via* direct faradaic electron transfer; whereby, addition of chloride ions enhanced Ag NP oxidative dissolution to Ag^+. NPs are often prepared in an IL using lithium borohydride ($LiBH_4$) as a reducing agent[30, 31, 33] and lack capping agents which can enhance their reactivity. However, Kanoufi's group[4] showed the presence of $LiBH_4$ nanocrystals (NCs), which formed from residual $LiBH_4$ after the tetrahydrofuran (THF) molecular solvent, used to deliver the $LiBH_4$, was removed under high vacuum with heating. NCs were detected by capacitive impacts at an immiscible aqueous|IL micro-interface.[4] Similarly, Banerjee *et al.* demonstrated that excess $LiBH_4$ likely helped stabilize metal NPs for long-term storage; however, it also behaved as a catalyst.[33] $LiBH_4$ is also of interest as an inorganic, solid-phase hydrogen storage alternative and in direct borohydride fuel cells *via* the $8e^-$ borohydride oxidation reaction (BOR).[34] Therefore, the electrocatalytic contribution of both $LiBH_4$ NCs and Pt NPs within an IL is of significant interest. These studies also highlight the need to understand the fundamental role that additions of molecular solvents to the IL phase play in solubility, chemical reactivity, and catalysis. ILs have been shown to possess a supramolecular structure with contact ion pairs or aggregates of IL ions.[35-38] Indeed, Bryant *et al.* recently proposed that ion aggregates act as templating regions for NP synthesis within ILs.[38]

Herein, $LiBH_4$ NCs as well as Pt and Au NPs were prepared in a tetraalkylphosphonium IL, trihexyltetradecylphosphonium bis(trifluorosulfonyl)imide ($P_{66614}NTf_2$). NC and NP impacts were recorded at a CF-UME. In the former, NC oxidation was shown to be aided by additions of THF, which is hypothesized to enhance the mobility of NPs and NCs as well as solubilize $LiBH_4$ and its oxidation products. This likely occurs by reducing the overall viscosity of the IL phase, but also by disrupting its supramolecular fluidic nature. Pt NPs were shown to electrocatalyze the BOR through ECA impacts.

2.3. Theory

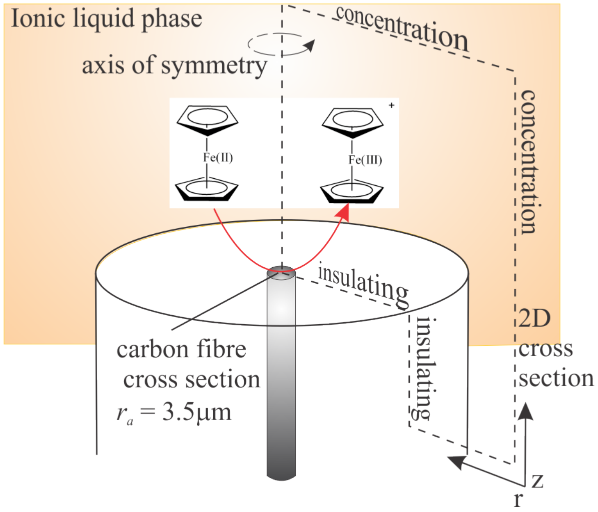

Figure 2.1: Illustration of the 2-dimensional, axial symmetric geometry employed within the Comsol Multiphysics Software as described by the dashed line. The boundary conditions are indicated along the outside edges, such that the glass sheath surrounding the carbon fibre was considered insulating, while the outside boundaries were 'concentration' to represent the continuous solution. The electrode surface boundary contained the equations for Butler-Volmer kinetics for ferrocene (Fc) oxidation/reduction.

Simulations were performed using Comsol Multiphysics Software (version 5.6) employing finite element method in a 2-dimensional, axial symmetric geometry. The geometry has been described in detail elsewhere[39] and is shown schematically in Figure 2.1. However, briefly, the simulation consisted of one domain in which diffusion was calculated assuming Fick's laws as per,

$$\frac{\partial c_{i^z}\left(r,\varphi,z,t\right)}{\partial t}=D_{i^z}\nabla^2 c_{i^z}\left(r,\varphi,z,t\right)$$

$$\nabla^2=\frac{1}{r}\frac{\partial}{\partial r}\left(r\frac{\partial}{\partial r}\right)+\frac{1}{r^2}\left(\frac{\partial^2}{\partial\varphi^2}\right)+\left(\frac{\partial^2}{\partial z^2}\right) \tag{2.1}$$

Where D_{i^z} and c_{i^z} are the diffusion coefficient and concentration of species *i* with charge *z* and ∇^2 is the Laplacian operator presented in cylindrical coordinates. The heterogeneous electron transfer reaction (equation 2.1) at the electrode boundary was defined using Butler-Volmer kinetics with rate constants k_f and k_b for the forward and backward reaction detailed by equations 2.3 and 2.4, respectively,

$$\mathrm{Fc}\underset{k_b}{\overset{k_f}{\rightleftharpoons}}\mathrm{Fc}^{+}+e^{-} \tag{2.2}$$

$$k_f=k^o\exp\left[\left(1-\alpha\right)f\left(E_{appl.}-E^{o'}\right)\right] \tag{2.3}$$

$$k_b=k^o\exp\left[-\alpha f\left(E_{appl.}-E^{o'}\right)\right] \tag{2.4}$$

Where k° is the standard rate constant, α is the transfer coefficient, while $f = n\mathrm{F/RT}$ who are the usual thermodynamic constants with $n = 1$ electrons transferred. A quasi-reversible k° of 10^{-5} m s^{-1} and $\alpha = 0.5$ was optimized by overlaying simulated CVs onto experimental ones and used throughout unless otherwise indicated. $E_{appl.}$ and $E^{\circ\prime}$ are the applied potential, which was a triangular wavefunction,[40] and the standard redox potential for the Fc^+/Fc redox couple – assumed to be 0.6 V *vs.* the quasi-RE employed in the IL phase. The current at the electrode boundary was calculated by,

$$I = nF\int D_{i^z}\nabla^2 c_{i^z}\left(r,\varphi,z,t\right)rdrd\varphi dt \tag{2.5}$$

A triangular mesh was employed and optimized for an ideal case verified against the theoretical steady state current (i_{ss}) from equation 2.6 (described below) with $k^{\circ} = 1$ m s^{-1}, $\alpha = 0.5$, $c^*_{\mathrm{Fc}} = 1$ mM, and $D_{\mathrm{Fc}} = 10^{-9}$ m^2 s^{-1}, until the simulated i_{ss} varied by <0.1% versus the theoretical one.

2.4. Results and Discussion

Figure 2.2A dashed, purple and solid, red traces depict the initial cyclic voltammograms (CVs) recorded in 1.2 M $LiBH_4$ dissolved in $P_{66614}NTf_2$ using either a 25 μm diameter Pt or 7 μm diameter carbon fibre (CF) inlaid disc ultramicroelectrode (UME), respectively. In both cases, there is a large irreversible anodic wave with onset potentials at roughly 1.0 and 1.7 V (*vs.* quasi-RE) at Pt and CF UMEs, respectively, that is not present in the absence of $LiBH_4$ (black, dashed curve in Figure 2.2A); therefore, this response is likely the borohydride oxidation reaction (BOR). Assuming a hemispherical diffusion regime where the magnitude of the steady state current (i_{ss}) for an inlaid disc electrode is described by,[41, 42]

$$i_{ss} = 4nFD_j c^*_j r_d \tag{2.6}$$

where r_d is the electrode radius, n is the number of electrons transferred, F is Faraday's constant, D_j is the diffusion coefficient of species j, and c^*_j is the initial/bulk concentration of species j. Thus, one can calculate the expected i_{ss} assuming a modest diffusion coefficient for BH_4^- in $P_{66614}NTf_2$ of 1×10^{-11} m^2 s^{-1} to be 16 and 57 nA at the CF and Pt UME, respectively. The latter is in fair agreement with the anodic steady state curve in Figure 2.2A; however, the CF UME response is much lower than expected and peak-shaped. While BOR is a multi-step process that is highly pH dependent, the overall reaction can be described generally by equations 2.7 and 2.8 in the case of direct oxidation or hydrolysis, respectively,[4, 43-45]

$$LiBH_4 + 8OH^- \rightarrow LiBO_2 + 6H_2O + 8e^- \tag{2.7}$$

$$LiBH_4 + (2+x)H_2O \rightarrow LiBO_2{\cdot}xH_2O + 4H_2 \tag{2.8}$$

Moreover, it has been shown that solubility within an IL is enhanced when the solute is a salt/ionic and shares a common ion with the IL, or suppressed if it does not.[46] Additionally, the viscosity of $P_{66614}NTf_2$ was observed to be higher qualitatively in the presence of $LiBH_4$. Moreover, as previously shown by Kanoufi's group using Back-Absorbing-Layer-Microscopy (BALM),[4] the $LiBH_4$ oxidation products deposit onto the surface of the electrode and are likely insoluble themselves, passivating the electrode.

During borohydride oxidation at the Pt UME, a cross-over event was recorded in the CV during the return, cathodic scan at ~2.6 V (Figure 2.2A). Such events are common in fuel cell investigations using Pt based anodes where large overpotentials often lead to oxidation of surface bound carbon monoxide, afterwards, and during the return scan, the Pt surface is free of -CO making the electrode more electrocatalytically active.[47-49] Previous reports have also recognized that Pt electrodes and NPs are good electrocatalytic surfaces for BOR.[4, 43, 44] However, no current enhancement was observed at the Pt UME. Both the lack of a steady state current profile at the CF UME and absence of current enhancement at the Pt UME can be explained by a passivation mechanism caused by the borohydride oxidation products. This mechanism likely also explains the unconventional shape of the *i-V* response recorded at the Pt UME.

Figure 2.2A(a) also shows the CV responses for the second and third scans (green and blue traces, respectively) at a CF UME immersed in 1.2 M $LiBH_4$ in $P_{66614}NTf_2$. With successive scans the borohydride oxidation peak at roughly 2.5 V (*vs.* quasi-RE) decreases which agrees with an electrode surface being passivated. Figure 2.2A(b) shows magnified plots of the third scan in the presence so $LiBH_4$ as well as the dashed, black trace without $LiBH_4$ added. These data could also suggest that the local concentration of $LiBH_4$ in the vicinity of the UME is irreversibly oxidized and consumed. This may be due to the high viscosity[50] of the IL or alternatively, as discovered recently by Kanoufi's group,[4] $LiBH_4$ could be sequestered as nanocrystals (NCs) within the IL phase.

Therefore, the lack of catalytic current enhancement at the Pt UME and the peak-shaped wave and lower-than-expected current response at the CF UME are likely due to two factors: (i) the generation of $LiBH_4$ oxidation products that passivate the electrode surface, and (ii) $LiBH_4$ being bound as NCs lowering the dissolved BH_4^- concentration.

The voltammetric response of 5 mM ferrocene (Fc) dissolved in $P_{66614}NTf_2$ in the presence of 1.2 M $LiBH_4$ is shown in Figure 2.2B, where the red, blue, and green curves are for the first to third scan, while the black, dashed curve is in the absence of $LiBH_4$. In the absence of $LiBH_4$, the Fc^+/Fc redox response is reversible and during the anodic scan follows a steady state current response. For simplicity, the potential scale in Figure 2.2B has been referenced to the Fc redox couple (Fc^+/Fc).[51, 52] The large peak-shaped response in the presence of $LiBH_4$ in scan 1 that decreases in magnitude with subsequent scans is likely owing to the re-reduction of Fc^+ to Fc by dissolved BH_4^- nearby the electrode surface through an EC′ mechanism (see Figure 2.2C, E =

electrochemical and C′ = catalytic). Again, LiBH$_4$ oxidation products (*e.g.*, LiBO$_2$) passivate the electrode surface resulting in a peak-shaped wave during the initial scan and a decrease in the current signal with subsequent scans.

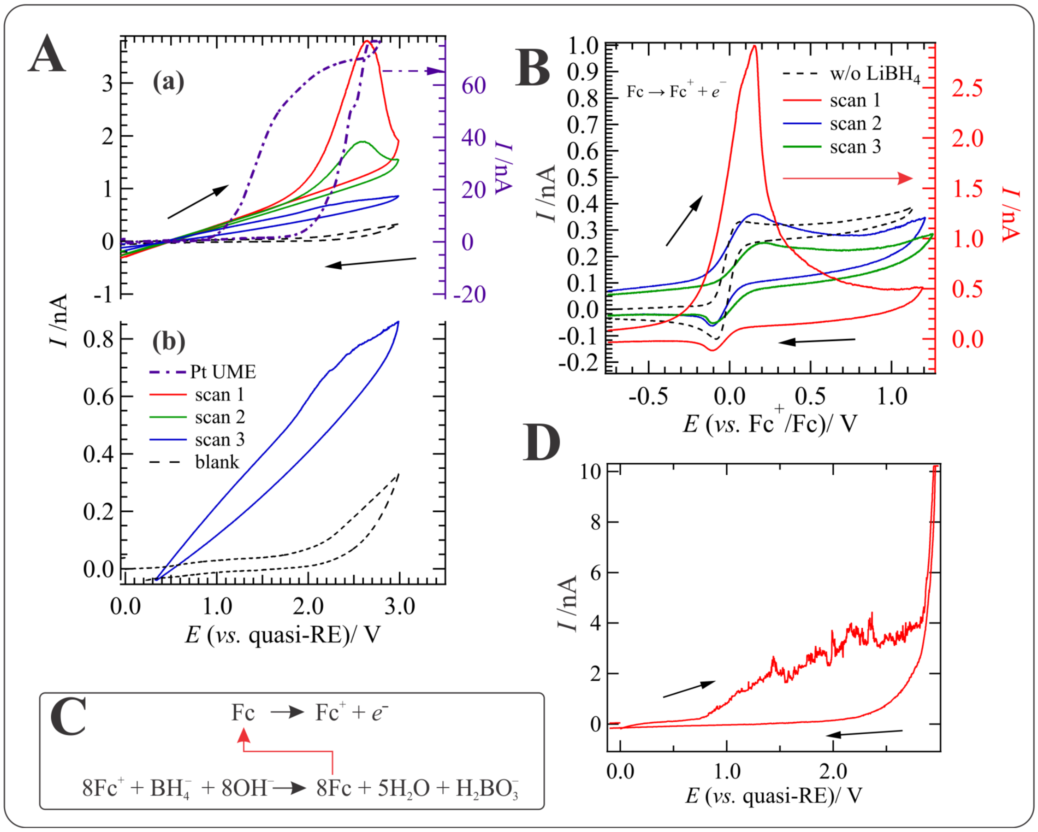

Figure 2.2: (A, a) Cyclic voltammograms (CVs) recorded using an inlaid disc ultramicroelectrode (UME) in P$_{66614}$NTf$_2$ with 1.2 M LiBH$_4$; the purple, dash-dot curve was performed using a 25 µm diameter Pt UME (first scan), while all other CVs were recorded using a 7 µm diameter carbon fibre (CF) UME, including the 1st to 3rd scans as indicated inset. (b) Contains magnified plots of the 3rd scan at a CF UME and the black, dashed curve that was measured without LiBH$_4$ added from (a). (B) CVs obtained using 5 mM ferrocene (Fc) in P$_{66614}$NTf$_2$ in the presence of 1.2 M LiBH$_4$ for the 1st to 3rd scans (red, blue, and green curves, respectively), as well as without LiBH$_4$ (black dashed line) using a CF UME; red arrow indicates the 1st scan plotted against the right-axis.

(C) EC′ (E = electrochemical, C′ = catalytic) mechanism of Fc re-reduction by BH_4^- in the vicinity of the UME during the *i*-V scans depicted in Figure 2B. (D) CV response with 1.2 M $LiBH_4$ in $P_{66614}NTf_2$ after addition of 40 μL of THF in air. A scan rate of 0.050 V s^{-1} was used throughout; black, solid arrows indicate scan direction, while the dashed, purple and solid red arrow indicates the axes plotted against.

After addition of 40 μL of THF to 1 mL of the 1.2 M $LiBH_4$ in $P_{66614}NTf_2$ solution (Figure 2.2D), current oscillations could be observed beginning at ~1.0 V (*vs.* quasi-RE) during the forward, anodic scan. It was hypothesized that these could be owing to $LiBH_4$-NC impact events that were made possible by THF either lowering the overall viscosity of the IL phase or enhancing the solubility of $LiBH_4$ and $LiBO_2$ by disrupting the IL supramolecular structure. To quantify the change in viscosity (η) the Stokes-Einstein equation was used along with Fc dissolved in the IL phase,

$$\eta = \frac{k_B T}{6\pi D_j r_j} \tag{2.9}$$

where k_B is the Boltzmann constant (1.381×10^{-23} J K^{-1}) and r_j is the hydrodynamic/spherical radius of the electroactive/solute species, in this case, Fc. The hydrodynamic radius is affected by numerous factors, such as solvent effects;[53] however, as a first approximation the value determined by Compton's group (~0.32 nm),[54, 55] which is near the crystallographic radius (0.27 nm) of Fc was employed.[56] With this in mind, the system was monitored using cyclic voltammetry and chronoampermetry where the latter were fit using the following function developed by Shoup and Szabo,[50, 57]

$$I = 4nFD_j c_j^* r_d f(\tau)$$
$$f(\tau) = 0.7854 + 08863\tau^{-1/2} + 0.2146e^{-0.7823\tau^{-1/2}} \qquad (2.10)$$
$$\tau = {4Dt}/{r_d^2}$$

Where t is time and τ is a dimensionless coefficient.

Figure 2.3A-C shows the CVs obtained after 0, 40, and 100 µL additions of THF to 1 mL of IL; inset in Figure 2.3A is an example of the CA recorded by applying a potential step from 0 to 1.0 V (*vs.* quasi-RE) and curve fit using equation 2.10.

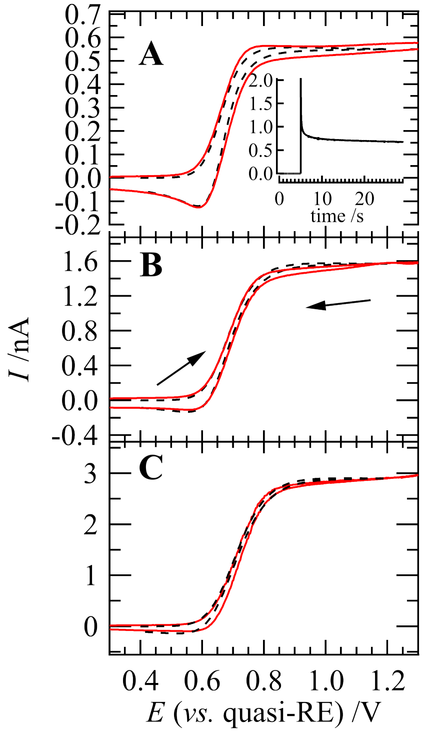

Figure 2.3: Red traces are CVs recorded using a CF UME (r_d = 3.5 µm) immersed in 1 mL of $P_{66614}NTf_2$ containing 10 mM of Fc at a scan rate of 0.020 V s^{-1} with no THF added (A) and after

40 (B) and 100 μL (C) additions of THF. Inset in (A) is an *i-t* potential-step from 0 to 1.0 V (*vs.* quasi-RE). Black dashed traces are simulated responses according to the Comsol program described in above while changing D_{Fc} and D_{Fc^+} as detailed in Table 2.1.

CVs in Figure 2.3 show a sigmoidal wave during the anodic scan which is indicative of radial diffusion to the inlaid disc UME; however, at low THF volumetric additions the backward cathodic scan has a peak-shape. It has been shown that asymmetries frequently arise in the diffusion coefficients between the oxidized and reduced forms even in molecular solvents. Martin and Unwin demonstrated that chronoamperometric recordings during scanning electrochemical microscopy (SECM) probe approach curves can be sensitive to unequal diffusion coefficients in relatively low viscosity molecular solvents like acetonitrile.[58] These results were later extended to IL/electrode interfaces in which the magnitude of the difference in D_j between oxidized and reduced forms can increase dramatically.[59, 60] Indeed, these data are similar to those observed by Buzzeo *et al.*[60] for one e^- reduction of O_2 $[O_2 + e^- \rightleftharpoons O_2^-]$ in an imidazolium and tetraalkylammonium IL in which D_{O_2} was determined to be two orders of magnitude greater than $D_{\mathrm{O}_2^{-\cdot}}$, *i.e.*, 1.48×10^{-10} m^2 s^{-1} *vs.* 4.66×10^{-12} m^2 s^{-1}, in the latter, tetraalkylammonium IL. To achieve the peak-shaped response during the backward, cathodic scan, D_{Fc^+} was set to an order of magnitude smaller than D_{Fc} in the Comsol simulation, *e.g.*, 0.03 and 0.39×10^{-10} m^2 s^{-1} for D_{Fc^+} and D_{Fc}, respectively. Table 2.1 provides a list of the results from the voltammetric and chronoamperometric investigation of the Fc$^+$/Fc redox couple including, i_{ss} obtained from the anodic CV scan, the diffusion coefficients calculated using equation 2.9 (D-i_{ss}), D determined from curve fitting the chronoamperogram (CA) using equation 2.10 (Shoup and Szabo[57]), as well as D_{Fc} and $D_{\mathrm{Fc^+}}$ optimized from overlays of simulated CV curves onto the experimental ones (see Figure 2.3 dashed curves). The values of D_{Fc} where in good agreement across the three different methods. η was calculated for each THF addition using D_{Fc} and $D_{\mathrm{Fc^+}}$ determined from the simulation. Interestingly, η calculated using $D_{\mathrm{Fc^+}}$ for no THF added is very close to the previously measured viscosity of $\mathrm{P_{66614}NTf_2}$, 332.3 mPa s,[50] and close to the manufacturer listed value. Nevertheless, these data provide a semi-quantitative measure of the change in viscosity with small additions of a polar organic solvent; whereby, after a 1% (v/v%) addition, the viscosity of the mixture has decreased by 50% *vs*. the IL alone, while after 10% (v/v%) addition, the viscosity has decreased 85%.

Table 2.1: Results from the Fc^+/Fc voltammetric/chronoamperometric and computational investigation shown in Figure 2.3. Here, i_{ss} refers to the experimental steady state current for Fc oxidation for each volume of THF added to the 1 mL solution in $P_{66614}NTf_2$. Diffusion coefficients were determined using the experimental steady state current (D-i_{ss}) and curve fitting of the *i-t* response with the method by Shoup and Szabo,[38,58] as well as from the Comsol simulation (sim.) for both Fc and Fc^+ as indicated. Viscosity (η) was calculated using the Stokes-Einstein equation as described in the main text using both D_{Fc} and D_{Fc^+} obtained from the simulated CV overlays.

Vol. THF added /µL	i_{ss} **/nA**	D **×10^{-10} m^2/s**				η **(mPa s) Fc (sim.)**	η **(mPa s) Fc$^+$ (sim.)**
		D-i_{ss}	**Shoup & Szabo[38,58]**	**Fc (sim.)**	**Fc$^+$ (sim.)**		
0	0.5355	0.395	0.38	0.39	0.03	26	341
10	1.045	0.774	0.49	0.7	0.06	15	171
20	1.103	0.817	0.65	0.83	0.09	12	114
30	1.515	1.121	0.89	1.1	0.1	9.3	102
40	1.54	1.14	1	1.13	0.1	9.1	102
50	2.216	1.64	1.1	1.6	0.16	6.4	64
60	2.265	1.677	1.5	1.68	0.17	6.1	60
70	2.238	1.657	1.5	1.68	0.17	6.1	60
80	2.622	1.941	1.6	1.9	0.2	5.4	51
90	2.63	1.947	1.8	1.9	0.2	5.4	51
100	2.842	2.104	1.8	2.1	0.2	4.9	51

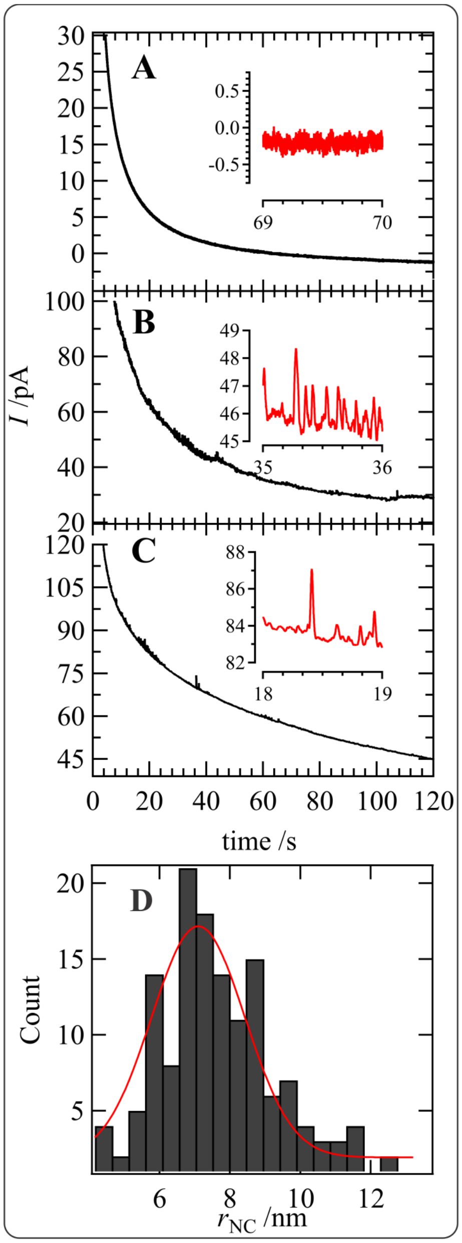

Figure 2.4: Chronoamperograms (CAs) performed at 1.5 V (*vs*. quasi-RE) using a CF UME (7 µm diameter) with 1.2 M $LiBH_4$ in $P_{66614}NTf_2$ as well as with 0, 20, and 40 µL of THF added for panels A-C in air. Inset are magnified segments of the respective *i-t* response curves. [D] Histogram of r_{NC} calculated using equation 2.11 and the integration of the peaks in the *i-t* response curves from panel B 20 µL injection of THF. The red trace is the product of a Gaussian curve fitting.

To further investigate the presence of NC impact events, CAs were recorded in $P_{66614}NTf_2$ solutions of 1.2 M $LiBH_4$; Figure 2.4 depicts the *i-t* curves obtained with 0 (A), 20 (B), and 40 μL (C) of THF added to the IL phase when exposed to air. Without THF added, no current oscillations were observed and the root mean square (rms) of the noise, ±0.197 pA (Figure 2.4A, inset), could be determined; see the Appendix A for details on rms calculation. However, after addition of 20 or 40 μL, the frequency (f) of the proposed impacts increased. Within the first 60 seconds an $f = 2.0\ s^{-1}$ was observed, which shifted to $0.4\ s^{-1}$ in the region of 60-120 s for the 20 μL THF addition. This agrees with the passivation of the electrode surface described above by the borohydride oxidation products. In between THF additions the UME was removed and polished using alumina oxide polishing pads. The frequency showed little change with subsequent additions of THF, 1.15 versus $1.2\ s^{-1}$ over the 120 s pulse duration for the 20 and 40 μL additions, respectively. The relatively constant frequency is likely owing to the highly dynamic environment and reactivity of the NC; whereby, as they decrease in size, more $LiBH_4$ becomes solubilized and the effective NC concentration decreases counteracting any increased mobility the NC gain as their average radius (r_{NC}) decreases. While speculative, this could be confirmed by *in situ* optical monitoring; however, this is beyond the scope of the present work. By integrating the *i-t* transient of each impact event, the charge transferred (Q) can be calculated and is related to r_{NC}, assuming they are perfectly spherical,[2, 4, 28, 61] by,

$$Q \propto \frac{\frac{4}{3}\pi r_{NC}^{3} n \rho F}{M_w} \tag{2.11}$$

where n was assumed to be ~8 based on equation 2.7, ρ is the density of $LiBH_4(s)$ (0.666 g cm^{-3}), and M_w is the molecular weight of $LiBH_4$ (21.84 g mol^{-1}). In this way, the histogram in Figure

2.4D, was obtained for the 20 μL THF addition. The r_{NC} distribution was fit using a Gaussian equation which had a peak at 7.1 nm and represents the average NC radius. A subsequent addition of THF (40 μL total) resulted in a decrease in the average r_{NC} to roughly 5.7 nm (data not shown). Since the reaction vial was exposed to air, it is likely that the NCs were slowly being oxidized and reduced in size through homogeneous reaction with adsorbed atmospheric water.

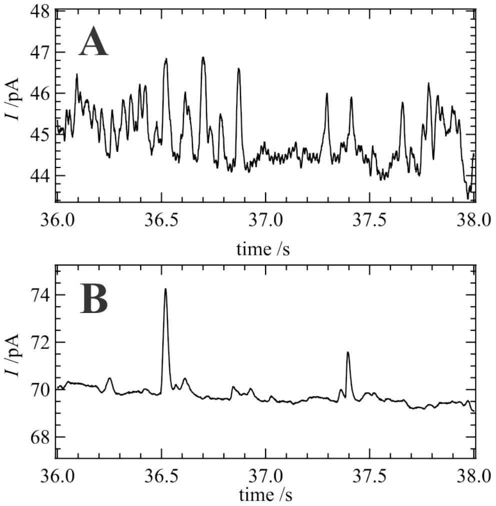

Figure 2.5: Magnified CAs illustrating peak-shape and duration from Figure 2.4 for 20 (A) and 40 μL (B) additions of THF.

Figure 2.5A and 2.5B show further magnified images of the CA curves from Figure 2.4 to illustrate further detail of the impact events. Typical impacts lasted between 0.020 s and 0.850 s with an average duration of ~0.112 s, which is well above the instrumental sampling interval/frequency of 800 μs/1250 kHz employed throughout.

Next, NP and NC in IL samples were imaged using TEM as described above. Figure 2.6A shows the TEM micrograph obtained after $PtCl_2$ reduction by $LiBH_4$ in $P_{66614}NTf_2$, and contains small

(~2.2 nm diameter), spherical Pt NPs which were of low dispersity. This Pt NP radius was used to calculate [Pt NP] assuming 100% conversion of $PtCl_2$. Figure 2.6B however, shows the larger $LiBH_4$ NCs present if the sampling solvent is carefully deoxygenated and sampled under inert atmosphere. $LiBH_4$ NCs were roughly spherical and averaged 5.1 nm in diameter, *i.e.*, r_{NC} = ~2.6 nm. Histograms of the NC diameter distribution have been shown inset in Figure 2.6 The $LiBH_4$ NC radii observed using TEM are roughly half that calculated using the oxidative, electrochemical impact analysis. This is likely owing to the highly reactive nature of the $LiBH_4$ NCs in molecular solvent and when exposed to water. Thus, some NCs are reduced in size during transfer to the TEM grid and their size is highly dynamic. These values are in fair agreement with those reported by Kanoufi's group,[4] *i.e.*, ~10 nm in diameter by TEM.

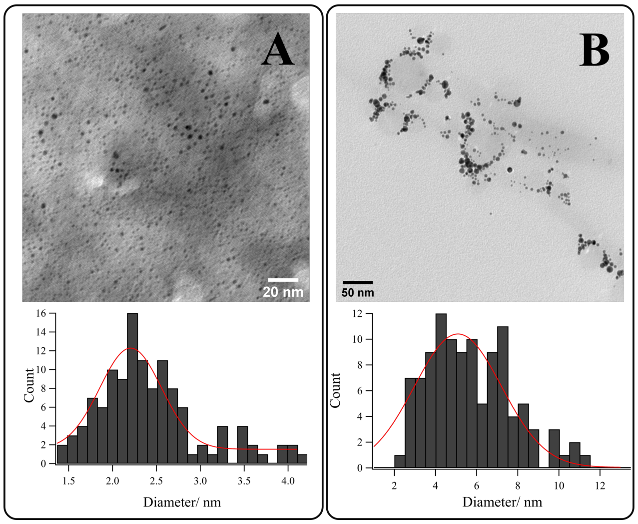

Figure 2.6: TEM micrographs of [A] Pt NPs and [B] $LiBH_4$ NCs. Inset are histograms of particle size distribution.

Moving forward, Figure 2.7 shows CAs recorded using a CF UME in the presence of varying concentrations of Pt NPs: 3.2×10^{16}, 1.0×10^{11}, and 1.3×10^{10} NP cm^{-3}, for panels A-C, respectively. In all cases there was an effective concentration of lithium borohydride, $[\mathrm{LiBH_4}]_{eff} \approx 1.2$ M. With Pt NPs present, current spikes were observed without needing to add THF, and the frequency of impacts increased concomitantly with Pt NP concentration; however, again, the frequency decreased with time. Using the viscosity of $\mathrm{P_{66614}NTf_2}$ (332.3 mPa s)[50] and the Stokes-Einstein relationship the diffusion coefficient (D_{NP}) of the Pt NPs was calculated, which in-turn was used to estimate the frequency (f) of impacts to an inlaid, planar UME by,[2, 61]

$$f = 4D_{\mathrm{NP}}c_{\mathrm{NP}}r_d \tag{2.12}$$

where r_d is the radius of the CF UME (3.5 μm) and c_{NP} is the NP concentration. In this way, the calculated frequencies at $c_{\mathrm{NP}} = 1\times10^{11}$ and 1.3×10^{10} NP cm^{-3} were 0.78 and 0.09 s^{-1}, while the experimentally observed values were 0.67 and 0.05 s^{-1}, respectively. While these values are in good agreement, the lower-than-expected experimental values agree with the proposed electrode passivation by $\mathrm{LiBH_4}$ oxidation products. These data, combined with previous reports for Pt electrocatalysis of BOR, indicate that the current spikes in Figure 2.7 are likely Pt NP stochastic impacts.

Figure 2.8 shows plots of the peak intensity (A) and duration (B) against their time of occurrence/location within the CA curve for [Pt NP] = 1.03×10^{11} Pt NP cm^{-3} (Figure 2.7B). The frequency of impacts decreases with time, along with the peak intensity; however, the duration of impact events remains high. These data agree with the proposed passivation mechanism that limits Pt NPs reactivity with each impact event. Inset are histograms depicting the distribution of peak intensities and durations which have been fit using a Gaussian equation with peaks at 4.9 pA and 0.093 s for Figures 2.8A and 2.8B, respectively. Figure 2.8C illustrates the plot of peak intensity versus duration; in which, there does not appear to be a significant correlation. Owing to the high frequency, [Pt NP] = 3.22×10^{16} Pt NP cm^{-3} (Figure 2.7A) could not be similarly analyzed as it was difficult to discriminate between impact events; however, [Pt NP] = 1.3×10^{10} Pt NP cm^{-3} was and demonstrated a similar trend (data not shown).

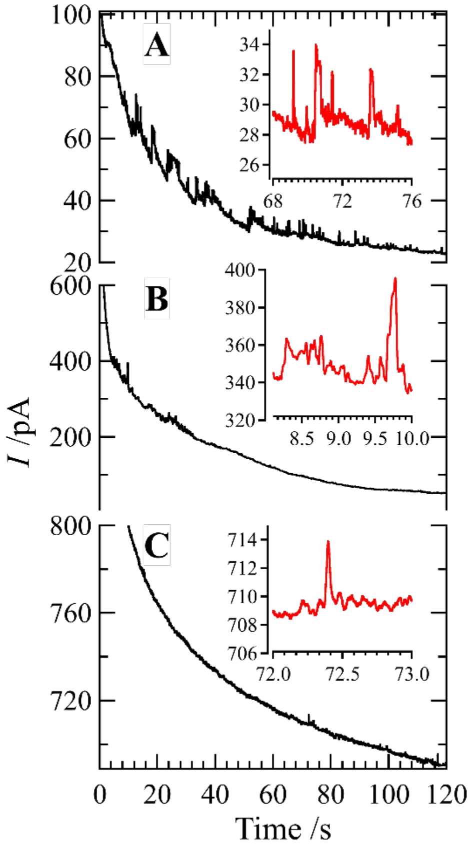

Figure 2.7: *i*-*t* responses recorded at an applied potential, *E* = 1.5 V (*vs*. quasi-RE) with the [Pt NP] equal to (A) 3.22×10^{16} (B) 1.03×10^{11} (C) 1.3×10^{10} Pt NP cm^{-3} in 1.2 M $LiBH_4$. Inset are magnified sections of the respective CA traces. All other experimental parameters are the same described in Figure 2.4.

By adding THF to the Pt NP/IL solution, the solubility of $LiBH_4$ is likely increased and the mobility of the Pt NPs are enhanced. Figure 2.9 shows that by adding 20 and 40 μL of THF the maximum current intensity of the current transient increases by a magnitude of roughly 2× and almost 50×, respectively. Robinson *et al.*[62] demonstrated that low ionic strength correlates with more single NP impacts and thus a decrease in particle aggregation. Thus, owing to the high ionic strength of the IL/THF solution, the large current spikes observed in Figure 2.9B are likely owing to the impacts of Pt NP agglomerates. The supramolecular fluidic nature of the IL seems to inhibit NP aggregation; however, these results suggest that it is quickly disrupted by only a relatively small (~1% v/v) addition of molecular solvent, which saw the largest decrease in η (see Table 2.1). Therefore, the large change in the catalytic enhancement for Pt NP impacts is likely owing to a fundamental disruption of the IL supramolecular fluidic nature that in turn promotes NP aggregation. Bryant *et al.*[38] recently demonstrated, using silylamine reversible ILs and DOSY-NMR, that the ion pairs/aggregates that form within the IL phase are responsible for the ILs supramolecular structure, as well as control NP nucleation and growth leading to small, low dispersity particles. The results herein, indicate that a small addition of polar organic solvent likely disrupts these IL ion-aggregates/clusters into smaller domains and may give rise to molecular solvent channels within the IL phase, since contact ion pairs have been shown to persist even at high IL dilutions.[63]

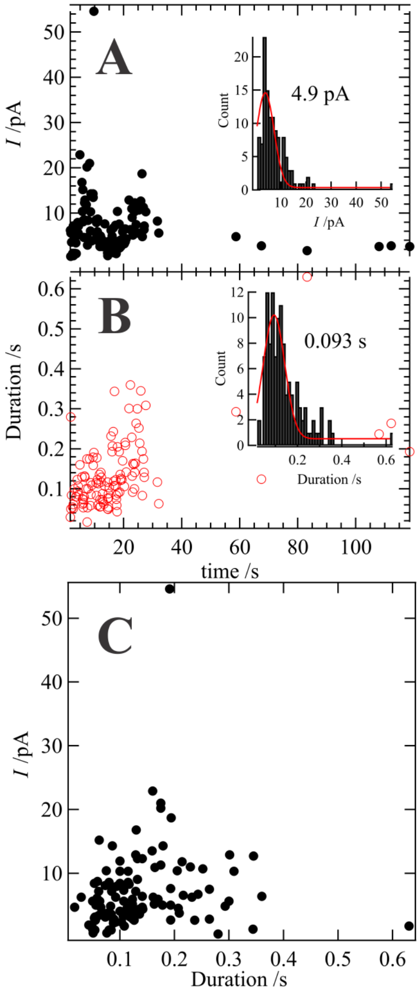

Figure 2.8: Panels A and B show plots of peak intensity and duration versus the time the impact event occurred, while C depicts peak intensity versus duration obtained from the *i-t* curve in Figure 2.7B at [Pt NP] = 1.03×10^{11} Pt NP cm^{-3}. Inset in A and B are histograms of peak intensity and duration, respectively, which include a Gaussian curve fitting (red trace); the peak value from each fitting has been written inset.

Interestingly, as highlighted inset in Figure 2.9 along with further magnified versions in Figure 2.10, Pt NP impacts are often accompanied by a current-step in the *i-t* profile. This is likely due to the Pt NP adsorbing onto the UME surface increasing the electroactive surface area; however, in this instance it is quickly overcome by the passivating affects of the BOR products. Figure A1 in the Appendix A shows histograms for the duration of impact events at $c_{NP} = 3.66\times10^{16}$ Pt NP cm^{-3} with 0%, 2%, and 4% v/v THF added, *i.e.*, CA curves drawn in Figures 2.7A, 2.9A, and 2.9B, respectively. Gaussian fittings for the 0 and 4% v/v THF histograms were possible and from their peaks an average duration of the impact events 0.015 and 0.008 s, respectively, were obtained. The maximum/minimum durations for 0, 2%, and 4% v/v THF were measured to be 1.08 s/0.0004 s, 3.30 s/0.0016 s, and 1.403 s/0.002 s, respectively, indicating a broad range of impact durations. As depicted in Figure 2.11, five peak shapes were classified, including ‘blocky’, sharp spike (traditional pattern), spike accompanied by a current step, a rolling spike, and a blunt spike. The change in duration is therefore linked to the change in frequency of these spike profiles which indicate the mechanism of NP interaction with the UME surface or may be linked to NP aggregation/changes in morphology.

Without THF added and at high [Pt NP] the *i-t* response is dominated by ‘blocky’ impact events. Owing to the high NP concentration, these may be owing to multiple consecutive impacts or a single NP impact which stays in proximity to the UME surface, effectively rolling or bouncing across electrode interface until it is either deactivated by the oxidation products or physically moves off into solution. At this stage it is not possible to distinguish between these two possibilities; however, the focus of future work will be to combine electrochemical measurements with optical ones, *i.e.*, darkfield optical microscopy or holography/NP tracking.[61] The neat Pt/IL NP solution also favours the ‘spike + current step’ profile versus the cases with THF added.

Once THF is added to the solution, the ‘blocky’ spike profile virtually disappears, and the traditional spike and blunt spike shape dominate. While the frequency of both is low at 2% and 4% v/v THF additions, as shown in Figure 2.9, they have the largest intensities and peak areas. These data indicate that NP aggregation is promoted with the loss of the ILs supramolecular nature. Lower intensity impact events in these cases tend towards the ‘rolling’ spike shape.

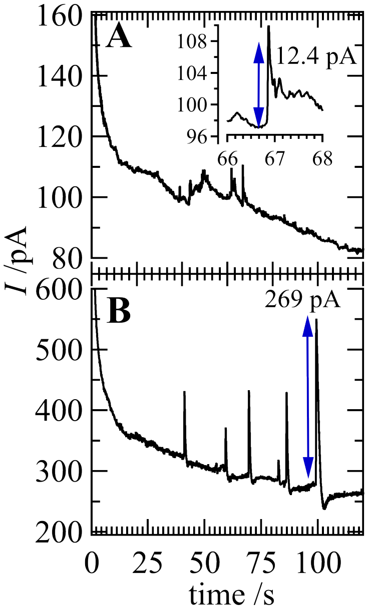

Figure 2.9: CA performed at 1.5 V (*vs*. quasi-RE) using a CF UME with $c_{NP} = 3.22\times10^{16}$ NP cm^{-3}, $[LiBH_4]_{eff} = 1.2$ M, in $P_{66614}NTf_2$ after (A) 20 and (B) 40 μL additions of dry THF added under air.

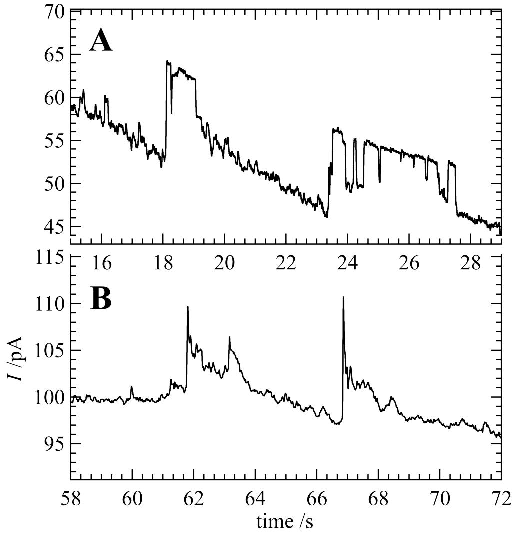

Figure 2.10: Magnified CAs from Figure 2.7A (A) and Figure 2.9B (B) for [Pt NP] 3.22×10^{16} NP cm^{-3}, [LiBH$_4$]$_{eff}$ = 1.2 M, in P$_{66614}$NTf$_2$ after 0 and 20 μL of THF added.

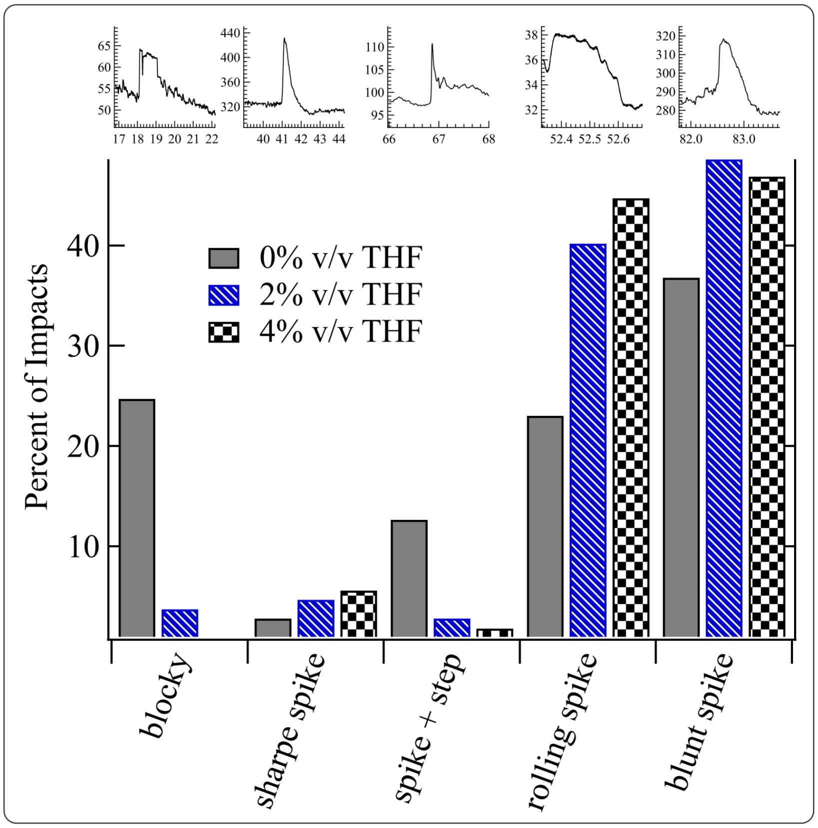

Figure 2.11: Breakdown of impact events observed at $c_{\mathrm{NP}} = 3.22\times10^{16}$ NP cm^{-3} for 0, 2%, and 4% v/v addition of THF to 1.2 M $LiBH_4$ in $P_{66614}NTf_2$. Inset and above are examples of the respective spike profiles.

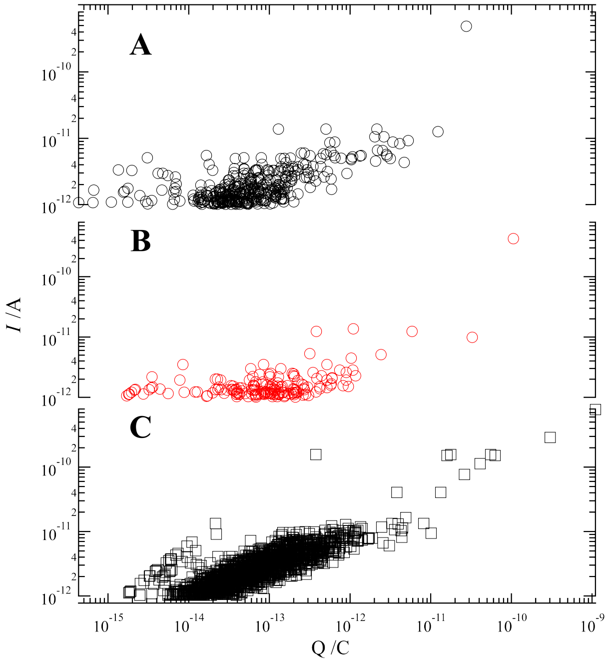

Figure 2.12: Plot of peak current versus charge transferred for $c_{NP} = 3.22\times10^{16}$ NP cm^{-3} for 0 (A), 2% (B), and 4% (C) v/v addition of THF to 1.2 M $LiBH_4$ in $P_{66614}NTf_2$ as obtained from analysis of *i*-*t* curves shown in Figures 2.7A, 2.9A, and 2.9B, respectively.

Figure 2.12 shows the plots of the peak current for each impact event versus the charge as obtained from integrating the *i*-*t* spike profile. The overall frequency of impacts for [Pt NP] = 3.22×10^{16} Pt NP cm^{-3} with 0, 2%, and 4% v/v THF added was 3.1, 1.4, and 13.8 s^{-1}; however, these data are coloured by the type of current spike. As the amount of THF increases, there is a concomitant increase in the intensity and amount of charge transferred, *i.e.*, $Q = \int idt$. Summing the total charge transferred for each impact across each 120 s pulse, one obtains 0.119, 0.176, and 1.903 nC for the respective 0%, 2%, and 4% v/v THF *i-t* curves. These results demonstrate the enhanced access to the UME surface and overall mobility that the Pt NPs gain with increasing molecular solvent. Using equation 2.7, assuming 100% conversion of $LiBH_4$ to $LiBO_2$, and that $LiBO_2$ will deposit as a disc 1.0 nm thick on the electrode surface, one obtains a radius of 0.01 μm for the smallest impact event, and a 9.03 μm radius for the largest. Since the UME surface is not immediately and complete passivated, these values indicate that the BOR oxidation products do not persist on the surface to a large degree. In Kanoufi's group's imaging experiments employing BALM,[4] the electrode surface was mounted with the solution phase on top and oxidation products were observed to disperse relatively evenly in a circular pattern surrounding the initial $LiBH_4$ NC. In this case, since the UME is inverted, it may prevent the electrode surface from becoming completely or permanently obscured. Alternatively, Pt NPs may accumulate on the UME and counterbalance the passivating affects of the BOR products by increasing the electrode surface area.

Assuming that the electrocatalytic activity of the Pt NPs is effectively countered by the passivating affects of the oxidation products and using equation 2.13 developed by Roland and Oldham[64] for a spherical microelectrode, one can calculate r_{NP},

$$i_p = 4\pi \ln\left(2\right) nFD_{\mathrm{LiBH_4}} c^*_{\mathrm{LiBH_4}} r_{\mathrm{NP}} \tag{2.13}$$

Where $D_{\mathrm{LiBH_4}}$ was calculated to be ~0.3 $\mu m^2 s^{-1}$ for the $LiBH_4$ NC, while $c^*_{\mathrm{LiBH_4}}$ was assumed to be equal to $[LiBH_4]_{eff} = 1.2$ M. While this is a gross estimate, from the peak current values for the $c_{\mathrm{NP}} = 3.66\times10^{16}$ NP cm^{-3} without THF added an average r_{NP} of 1.8 nm was calculated, which is in good agreement with the TEM images of the Pt NPs.

Au NPs prepared in a similar manner within $P_{66614}NTf_2$ were of low dispersity with an $r_{NP} \approx 3.7$ nm (see Figure A2 of the Appendix A). However, CA studies employing Au NPs did not elicit any current spikes (data not shown). However, this was expected since Au has been shown to be a poor catalyst for BOR.[34, 43] When these results are contrasted against the Pt NP ones above, it highlights the overall electrocatalytic activity of Pt NPs towards BOR.

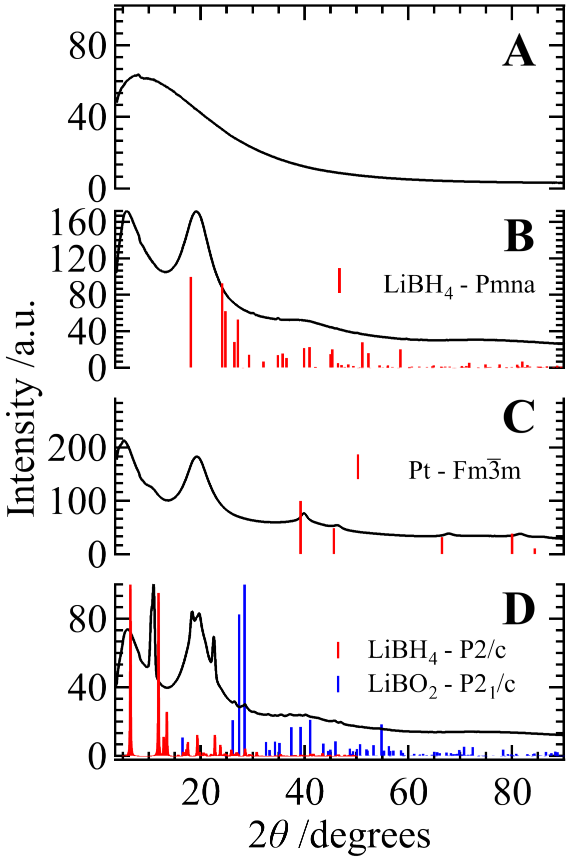

Figure 2.13: Black traces are X-ray diffraction (PXRD) spectra of neat $P_{66614}NTf_2$ (A); 1.2 M $LiBH_4$ in $P_{66614}NTf_2$ (B); 3.22×10^{16} Pt NPs cm^{-3}, 1.2 M $LiBH_4$ in $P_{66614}NTf_2$ (C); and 1.2 M $LiBH_4$ in $P_{66614}NTf_2$ after 30 min exposure to acetone (D). Red and blue stick plots are calculated PXRD spectra (obtained from https://materialsproject.org/) of the inorganic salt or metal for the space group indicated inset.

Figures 2.13A-C show powder X-ray diffraction (PXRD) spectra obtained for neat $P_{66614}NTf_2$ as well as $LiBH_4$ NC and $LiBH_4$ NC/Pt NP suspensions in $P_{66614}NTf_2$, respectively. Meanwhile, Figure 2.13D shows the PXRD spectrum obtained after 1.2 M $LiBH_4$ in $P_{66614}NTf_2$ was treated with an excess of acetone for 30 min with stirring in air, which was subsequently removed under high vacuum with heating overnight. The $LiBH_4$ NCs in $P_{66614}NTf_2$ spectra has a single broad peak at roughly 19° 2θ, that is present in all other spectra and is close to the calculated peak for $LiBH_4$ in the Pmna space group at 18.02° 2θ – red curve overlaid in Figure 2.13B. Similarly, in Figure 2.13C, signals closely matching calculated Pt values were observed; however, the experimental values were broad and positively shifted relative to their expected values. This is likely due to Pt NPs being so small (~2 nm in diameter) and signal attenuation owing to the IL environment. The shift in experimental peak values relative to the calculated ones increases concomitantly with increasing 2θ, which indicates that this is not owing to sample misalignment or displacement but a feature inherent to the particles.

Interestingly, after washing the sample of $LiBH_4$ NCs ($[LiBH_4]_{eff}$ = 1.2 M) in $P_{66614}NTf_2$ with acetone for 30 min, then removing acetone and any volatile reduction products (*e.g.*, isopropanol, propane) under vacuum, the PXRD spectra still showed signs of $LiBH_4$ (Figure 2.13D) along with possible oxidation products (*e.g.*, $LiBO_2$, $B(OH)_3$). A peak at ~10° 2θ is close to the calculated peak for $LiBH_4$ in the P2/c space group at 11.82° 2θ; however, similar to the case of Pt NPs in $P_{66614}NTf_2$ above, there is a slight shift in the peak position. Large white crystals could be observed using an optical microscope suspended in the IL phase after acetone treatment. Thus, treating the $LiBH_4$ NC/$P_{66614}NTf_2$ solution promoted NC aggregation which inhibited their oxidation and effectively acted as a kind of recrystallization. These larger crystals are likely responsible for the shift in character of the principal peak at ~18.0° 2θ. While these PXRD results are surprising and raise numerous other questions about the IL environment and NP/NC structure, these are beyond the scope of this work.

2.5. Conclusions

Using $P_{66614}NTf_2$ IL as the solvent for NP and NC preparation, Pt and Au NPs as well as $LiBH_4$ NCs were prepared. Pt NP impacts were recorded through ECA of the BOR, while Au NPs demonstrated no catalytic activity towards the BOR, both in agreement with previous reports.[34, 43] $LiBH_4$ NC impacts were detected by a direct oxidative pathway whose products (*e.g.*, $LiBO_2$) passivate the UME surface.

Critically, THF, a model, polar molecular solvent enhances the solubility $LiBH_4$ NC, while simultaneously disrupting the supramolecular structure of the IL promoting NP agglomeration. This was observed as an enhancement in the ECA signal for Pt NP mediated BOR. These findings will be of considerable interest to the IL and catalytic communities since combinations of ILs and NPs are being used as catalyst substrates for organic reactions. Small additions of the starting materials, often polar solvents themselves, likely disrupt the IL/NP behaviour in a similar fashion and can alter their overall reactivity, which may be advantageous.

2.6. Experimental Section

All chemicals were used as received without any additional purification unless otherwise indicated. Lithium bis(trifluoromethylsulfonyl)imide ($LiNTf_2$, 99.95%), Trihexyltetradecylphosphonium bromide (≥95%), potassium tetrachloroaurate ($KAuCl_4$, >98%), lithium borohydride solution (2.0 M in THF), lithium sulfate monohydrate (≥99%), ferrocene (bis(cyclopentadienyl)iron(II), >98%) were obtained from Sigma-Aldrich. Platinum (II) chloride (98%) was purchased from Alfa Aesar. Dichloromethane (≥99.5%) and acetone (≥99.5%) were sourced from ACS. Tetrahydrofuran (THF) and toluene were acquired from an MBraun solvent purification system, sparged using dry N_2 gas and dried over activated alumina. Ultrapure water from a MilliQ filtration system (>18.2 MΩ cm) was used for making aqueous solutions.

$P_{66614}NTf_2$ was prepared by metathesis reaction as previously described.[50, 65, 66] The final viscous, clear liquid was structurally confirmed through ^{1}H NMR.

Pt nanoparticles (NPs) were prepared in the ionic liquid (IL) phase using a modified method outlined by Banerjee *et al*.[31, 33] 5 mg $PtCl_2$ was added to 1 mL $P_{66614}NTf_2$ and heated to 60°C under N_2 gas. Then, 600 μL of 2.0 M $LiBH_4$ in tetrahydrofuran (THF) was added dropwise over 5 min. Subsequently, the reaction vessel was heated to 80°C and the THF was removed under vacuum overnight. The final solution was black and Pt NP size was confirmed by TEM. Au NPs were similarly generated, however, a dark red, “wine coloured” solution was obtained.

Transmission electron microscopy (TEM) images were acquired using a Tecnai Spirit transmission electron microscope. Samples were deposited onto 200 mesh Cu ultrathin/lacey carbon grids (Electron Microscopy Sciences) *via* suspension of the grid into a 1 mL solution of toluene containing a 10 μL aliquot of the NP/$P_{66614}NTf_2$ mixture. The grids were then dried under a flow of N_2.

All electrochemical results were recorded using a PG-618-USB potentiostat (HEKA Electroniks) in a 2-electrode mode; whereby, either a Pt or carbon fibre (CF) ultramicroelectrode (UME), 25 or 7 μm in diameter, respectively, were employed as the working electrode (WE) and a silver wire (Goodfellow Inc.) was used as the counter/quasi-reference electrode (CE/quasi-RE).

UME fabrication has been described elsewhere.[50, 67] Briefly, a 1-2 cm length of Pt wire or CF (Goodfellow Inc.) was placed into the open end of a pulled, tapered borosilicate glass capillary, pushed into place in the tapered end, and annealed in place under vacuum using an electric puller (Model# PC-100, Narishige). After sealing the wire with the heating coil, the UME was polished by using 12, 9, 3, 1, and finally 0.3 μm Buehler alumina oxide polishing pads using a custom build polishing wheel. Activated charcoal was added to the back/open end of the capillary to make the connection to a Cu wire and the WE lead of the potentiostat.

Powder X-ray diffraction (PXRD) data was performed on a XtaLAB Synergy-S, Dualflex, HyPix-6000HE diffractometer using Cu $K\alpha$ radiation (λ = 1.5406 Å). The power sample was mounted on a Nylon CryoLoop, and a series of 360° phi-scans over a period of 14 min were collected at room temperature. The data collection and extraction were processed within *CrysAlisPro* (Rigaku OD, 2021).

2.7. References

1. L. A. Baker, *J. Am. Chem. Soc.* **2018**, *140*, 15549-15559.
2. S. V. Sokolov, S. Eloul, E. Katelhon, C. Batchelor-McAuley, R. G. Compton, *Phys. Chem. Chem. Phys.* **2017**, *19*, 28-43.
3. X. Xiao, A. J. Bard, *J. Am. Chem. Soc.* **2007**, *129*, 9610-9612.
4. T. J. Stockmann, J.-F. Lemineur, H. Liu, C. Cometto, M. Robert, C. Combellas, F. Kanoufi, *Electrochim. Acta* **2019**, *299*, 222-230.

5. T. J. Stockmann, L. Angelé, V. Brasiliense, C. Combellas, F. Kanoufi, *Angew. Chem. Int. Ed.* **2017**, *56*, 13493-13497.

6. G. R. Willmott, *Anal. Chem.* **2018**, *90*, 2987-2995.

7. S. R. German, T. S. Hurd, H. S. White, T. L. Mega, *ACS Nano* **2015**, *9*, 7186-7194.

8. J.-F. Lemineur, J.-M. Noël, A. Courty, D. Ausserré, C. Combellas, F. Kanoufi, *J. Am. Chem. Soc.* **2020**, *142*, 7937-7946.

9. N. Nakatsuka, K.-A. Yang, J. M. Abendroth, K. M. Cheung, X. Xu, H. Yang, C. Zhao, B. Zhu, Y. S. Rim, Y. Yang, P. S. Weiss, M. N. Stojanović, A. M. Andrews, *Science* **2018**, *362*, 319.

10. J. E. Dick, A. T. Hilterbrand, L. M. Strawsine, J. W. Upton, A. J. Bard, *Proc. Natl. Acad. Sci* **2016**.

11. H. Wang, C. Yang, H. Tang, Y. Li, *Anal. Chem.* **2021**, *93*, 4593-4600.

12. H. Tang, H. Wang, J. Du, D. Zhao, M. Cao, Y. Li, *J. Phys. Chem. Lett.* **2021**, *12*, 5443-5447.

13. D. Perry, B. Paulose Nadappuram, D. Momotenko, P. D. Voyias, A. Page, G. Tripathi, B. G. Frenguelli, P. R. Unwin, *J. Am. Chem. Soc.* **2016**, *138*, 3152-3160.

14. D. J. Leszczyszyn, J. A. Jankowski, O. H. Viveros, E. J. Diliberto, Jr., J. A. Near, R. M. Wightman, *J. Biol. Chem.* **1990**, *265*, 14736-14737.

15. L. Sepunaru, S. V. Sokolov, J. Holter, N. P. Young, R. G. Compton, *Angew. Chem.* **2016**, *128*, 9920-9923.

16. C. Liu, P. Peljo, X. Huang, W. Cheng, L. Wang, H. Deng, *Anal. Chem.* **2017**, DOI: 10.1021/acs.analchem.1027b02072.

17. S. Kang, A. F. Nieuwenhuis, K. Mathwig, D. Mampallil, S. G. Lemay, *ACS Nano* **2013**, *7*, 10931-10937.

18. S. Kang, A. F. Nieuwenhuis, K. Mathwig, D. Mampallil, Z. A. Kostiuchenko, S. G. Lemay, *Faraday Discuss.* **2016**, *193*, 41-50.
19. J. W. Jordan, K. L. Y. Fung, S. T. Skowron, C. S. Allen, J. Biskupek, G. N. Newton, U. Kaiser, A. N. Khlobystov, *Chem. Sci.* **2021**, *12*, 7377-7387.
20. Y. Wang, X. Shan, N. Tao, *Faraday Discuss.* **2016**, *193*, 9-39.
21. E. Laborda, A. Molina, V. F. Espín, F. Martínez-Ortiz, J. García de la Torre, R. G. Compton, *Angew. Chem. Int. Ed.* **2017**, *56*, 782-785.
22. E. Laborda, A. Molina, *Curr. Opin. Electrochem.* **2021**, *26*, 100664.
23. H. Deng, P. Peljo, X. Huang, E. Smirnov, S. Sarkar, S. Maye, H. H. Girault, D. Mandler, *J. Am. Chem. Soc.* **2021**, *143*, 7671-7680.
24. J.-F. Lemineur, T. J. Stockmann, J. Médard, C. Smadja, C. Combellas, F. Kanoufi, *J. Anal. Test.* **2019**, *3*, 175-188.
25. V. Brasiliense, J. Clausmeyer, A. L. Dauphin, J.-M. Noël, P. Berto, G. Tessier, W. Schuhmann, F. Kanoufi, *Angew. Chem. Int. Ed.* **2017**, *56*, 10598-10601.
26. A. N. Patel, A. Martinez-Marrades, V. Brasiliense, D. Koshelev, M. Besbes, R. Kuszelewicz, C. Combellas, G. Tessier, F. Kanoufi, *Nano Lett.* **2015**, *15*, 6454-6463.
27. Y. Wang, Z. Tang, H.-Y. Chen, W. Wang, N. Tao, H. Wang, *Proc. Natl. Acad. Sci* **2021**, *118*, e2104598118.
28. E. Kätelhön, E. E. L. Tanner, C. Batchelor-McAuley, R. G. Compton, *Electrochim. Acta* **2016**, *199*, 297-304.
29. E. E. L. Tanner, C. Batchelor-McAuley, R. G. Compton, *J. Phys. Chem. C* **2016**, *120*, 1959-1965.

30. M. M. Seitkalieva, D. E. Samoylenko, K. A. Lotsman, K. S. Rodygin, V. P. Ananikov, *Coord. Chem. Rev.* **2021**, *445*, 213982.

31. A. Banerjee, R. Theron, R. W. J. Scott, *Chem. Commun.* **2013**, *49*, 3227-3229.

32. H. A. Kalviri, F. M. Kerton, *Green Chem.* **2011**, *13*, 681-686.

33. A. Banerjee, R. W. J. Scott, *Green Chem.* **2015**, *17*, 1597-1604.

34. G. Braesch, A. Bonnefont, V. Martin, E. R. Savinova, M. Chatenet, *Electrochim. Acta* **2018**, *273*, 483-494.

35. H. K. Stassen, R. Ludwig, A. Wulf, J. Dupont, *Chem. Eur. J.* **2015**, *21*, 8324-8335.

36. Y. Marcus, G. Hefter, *Chem. Rev.* **2006**, *106*, 4585-4621.

37. K. Damodaran, *Prog. Nucl. Magn. Reson. Spectrosc.* **2022**, *129*, 1-27.

38. K. Bryant, E. Hammond-Pereira, S. R. Saunders, *J. Phys. Chem. B* **2021**, *125*, 253-263.

39. T. J. Stockmann, Z. Ding, *J. Phys. Chem. B* **2012**, *116*, 12826-12834.

40. P. J. Rodgers, S. Amemiya, *Anal. Chem.* **2007**, *79*, 9276-9285.

41. D. W. M. Arrigan, *Analyst* **2004**, *129*, 1157-1165.

42. R. M. Wightman, *Anal. Chem.* **1981**, *53*, 1125A-1126, 1128A, 1130A, 1132A, 1134A.

43. M. V. Mirkin, H. Yang, A. J. Bard, *J. Electrochem. Soc.* **1992**, *139*, 2212-2217.

44. J. I. Martins, M. C. Nunes, R. Koch, L. Martins, M. Bazzaoui, *Electrochim. Acta* **2007**, *52*, 6443-6449.

45. G. Rostamikia, M. J. Janik, *Energy Environ. Sci.* **2010**, *3*, 1262-1274.

46. A. B. Pereiro, J. M. M. Araújo, F. S. Oliveira, J. M. S. S. Esperança, J. N. Canongia Lopes, I. M. Marrucho, L. P. N. Rebelo, *J. Chem. Thermodyn.* **2012**, *55*, 29-36.

47. S. Kar, A. Goeppert, G. K. S. Prakash, *Acc. Chem. Res.* **2019**, *52*, 2892-2903.

48. A. Sayadi, P. G. Pickup, *Russ. J. Electrochem.* **2017**, *53*, 1054-1060.

49. Y. Tan, C. Xu, G. Chen, N. Zheng, Q. Xie, *Energy Environ. Sci.* **2012**, *5*, 6923-6927.

50. T. J. Stockmann, J. Zhang, J. C. Wren, Z. Ding, *Electrochim. Acta* **2012**, *62*, 8-18.

51. A. Lewandowski, L. Waligora, M. Galinski, *Electroanalysis* **2009**, *21*, 2221-2227.

52. R. R. Gagne, C. A. Koval, G. C. Lisensky, *Inorg. Chem.* **1980**, *19*, 2854-2855.

53. C. O. Laoire, E. Plichta, M. Hendrickson, S. Mukerjee, K. M. Abraham, *Electrochim. Acta* **2009**, *54*, 6560-6564.

54. A. M. Bond, R. Colton, J. Harvey, R. S. Hutton, *J. Electroanal. Chem.* **1997**, *426*, 145-155.

55. S. R. Jacob, Q. Hong, B. A. Coles, R. G. Compton, *J. Phys. Chem. B* **1999**, *103*, 2963-2969.

56. J. B. Shotwell, R. A. Flowers II, *Electroanalysis* **2000**, *12*, 223-226.

57. D. Shoup, A. Szabo, *J. Electroanal. Chem. Interfacial Electrochem.* **1982**, *140*, 237-245.

58. R. D. Martin, P. R. Unwin, *J. Electroanal. Chem.* **1997**, *439*, 123-136.

59. P. Ugo, L. M. Moretto, M. De Leo, A. P. Doherty, C. Vallese, S. Pentlavalli, *Electrochim. Acta* **2010**, *55*, 2865-2872.

60. M. C. Buzzeo, O. V. Klymenko, J. D. Wadhawan, C. Hardacre, K. R. Seddon, R. G. Compton, *J. Phys. Chem. A* **2003**, *107*, 8872-8878.

61. V. Brasiliense, A. N. Patel, A. Martinez-Marrades, J. Shi, Y. Chen, C. Combellas, G. Tessier, F. Kanoufi, *J. Am. Chem. Soc.* **2016**, *138*, 3478-3483.

62. D. A. Robinson, A. M. Kondajji, A. D. Castañeda, R. Dasari, R. M. Crooks, K. J. Stevenson, *J. Phys. Chem. Lett.* **2016**, *7*, 2512-2517.

63. M. Zanatta, V. U. Antunes, C. F. Tormena, J. Dupont, F. P. dos Santos, *Phys. Chem. Chem. Phys.* **2019**, *21*, 2567-2571.

64. L. C. R. Alfred, K. B. Oldham, *J. Phys. Chem.* **1996**, *100*, 2170-2177.

65. U. Domańska, M. Wlazło, M. Karpińska, M. Zawadzki, *Fluid Phase Equilib.* **2018**, *475*, 89-94.

66. R. Moshrefi, A. Suryawanshi, T. J. Stockmann, *Electrochem. Commun.* **2021**, *122*, 106894.

67. T. J. Stockmann, Y. Lu, J. Zhang, H. H. Girault, Z. Ding, *Chem. Eur. J.* **2011**, *17*, 13206-13216.

Chapter 3

Electrochemical investigation of Pt NP impacts at a micro water|ionic liquid interface

3.1. Introduction

Studying the catalytic activity of metal-NPs has become a popular aspect of electrochemistry. Many studies have been done to determine NP dynamics and properties using stochastic collisions (*i.e.*, SEE) at a solid interface such as a UME.[1] Many kinds of organic and inorganic NPs have been investigated by this method.[2-5] NPs can be detected by adsorbing/blocking, direct oxidation, or indirectly by electrocatalysis of a redox reaction (see Section 1.1.2). The solid interface has many advantages for the detection of NPs; however, it is highly dependent on electrode surface size, roughness, and geometry.[6]

The immiscible, polarizable liquid|liquid interface (LLI) has been studied extensively as an electrochemical platform. Recently, the LLI has been used to investigate NPs. In comparison with the solid|liquid interface, NPs can be studied independently from electrode properties at the LLI.[7] Also, as is mentioned in Chapter 1, either ET or IT can be studied through the LLI, which is highly reproducible and easy to fabricate.[8] Through NP collisions at the LLI, they can be detected by either oxidation/reduction of the NPs themselves or by charge transfer reactions with the NP functioning as a mediator/reactive center. With regards to the latter and based on common convention, if a negative charge transfers from the aqueous phase to the organic phase or a positive charge transfers from the organic phase (o) to the aqueous phase (w), then the peak current would be negative. However, if negative charge transfers from o→w or positive charge transfer from w→o, then the peak current would be positive. Stockmann *et al.*[9] detected Pt NP impacts by their electrocatalysis of the oxygen reduction reaction (ORR) at a micro water|1,2-dichloroethane (w|DCE) interface. They could study the Pt NPs features as electrocatalysts for ORR through this method. They also proposed that from testing the different sizes of NPs, the bigger Pt NPs penetrated the LLI more deeply, while smaller ones rested on the surface, *i.e.*, little to no penetration.

Another example was repeated by Gründer *et al.*[7] in 2013. They uncovered the catalytic activity of Au and Pd shell for Au NPs for ORR at LLI by adsorbing NPs at the w|DCB (1,2 dichlorobenzene) interface. Using this method, they found that the catalytic activity of the Au-Pd core-shell is much higher than Au NPs due to the larger area for adsorbing hydrogen.

In this chapter, preliminary electrochemical investigations of the catalytic activity of Pt NPs at a w|IL micro-interface towards both the borohydride oxidation reaction (BOR) and methanol oxidation reaction are described. The LLI was formed between $P_{66614}NTF_2$ and water. $P_{66614}NTF_2$ was chosen because it is hydrophobic[10] and immisible in water.

3.2. Theoretical

In electrochemical studies at LLIs, an electrode is immersed in either phase, in general α or β, with inner potentials ϕ_α or ϕ_β, respectively. Thus, a potential difference across the interface between the two phases develops and can be described by equation 3.1:[11-12]

$$\Delta_\alpha^\beta \phi = \phi_\beta - \phi_\alpha \tag{3.1}$$

Simple ion transfer of species *i* with charge z_i can similarly be written as,[13]

$$i_{\alpha}^{z_i} \rightleftharpoons i_{\alpha}^{z_i} \tag{3.2}$$

The electrochemical potential ($\tilde{\mu}_{\alpha,i}$)[13] is defined as,

$$\tilde{\mu}_{\alpha,i} = \mu_{\alpha,i}^{0} + RT\ln\left(a_{\alpha,i}\right) + z_i F\phi_{\alpha} \tag{3.3}$$

where F is Faraday's constant, R is the universal gas constant, and T is temperature in Kelvin. The parameters $\mu_{\alpha,i}^{o}$ and $a_{\alpha,i}$ are the standard chemical potential and activity of ion *i* in phase α. By assuming the interface is between water and oil, α and β can be replaced with w and o. Thus, by combining Equations 3.1 and 3.3, one can obtain equation 3.4,

$$\Delta_{o}^{w}\phi = \phi_{w} - \phi_{o} = \frac{\mu_{w,i}^{0} - \mu_{o,i}^{0}}{z_i F} + RT\, ln\frac{a_{w,i}}{a_{o,i}} \tag{3.4}$$

If one assumes that *a* ≈ *c* (the concentration of species *i*), then,

$$\Delta_{\mathrm{o}}^{\mathrm{w}}\phi = \Delta_{\mathrm{o}}^{\mathrm{w}}\phi_{\mathrm{i,tr\;w\to o}}^{\mathrm{o}} + \frac{\mathrm{RT}}{\mathrm{z_i F}}\ln\left(\frac{c_{\mathrm{w,i}}}{c_{\mathrm{o,i}}}\right) \tag{3.5}$$

Where $\Delta_{\mathrm{o}}^{\mathrm{w}}\phi_{\mathrm{i,tr\;w\to o}}^{\mathrm{o}}$ is the standard ion transfer potential and defined as,

$$\Delta_{\mathrm{o}}^{\mathrm{w}}\phi_{\mathrm{i,tr\;w\to o}}^{\mathrm{o}} = \frac{\mu_{\mathrm{w,i}}^{\mathrm{o}} - \mu_{\mathrm{o,i}}^{\mathrm{o}}}{\mathrm{z_i F}} = \frac{\Delta \mathrm{G}_{\mathrm{i,tr\;w\to o}}^{\mathrm{o}}}{\mathrm{z_i F}} \tag{3.6}$$

and $\Delta\mathrm{G}_{\mathrm{i,tr\;w\to o}}^{\mathrm{o}}$ is the standard Gibbs energy of ion transfer of *i* from water to the organic phase: equation 3.5 is the Nernst equation for simple ion transfer at a LLI.

3.3. Experimental

See Section 2.4 for chemical reagents and experimental details.

The following electrochemical cell was used:

$$\mathrm{Au|Au_2(SO_4)_3}\left|\mathrm{5mM\ Li_2SO_4(aq)}\right\|\begin{matrix}\mathrm{x\ Pt\ NPs}\\ \mathrm{xM\ LiBH_4}\end{matrix}\ \mathrm{(P_{66614}NTf_2)}\left|\mathrm{AgNTf_2}\right|\mathrm{Ag} \qquad \textbf{Cell 1}$$

3.4. Results and Discussion

At first, the system without Pt NPs was investigated. Figure 3.1 shows the CV recorded for 1.2 M $LiBH_4$ dissolved in $P_{66614}NTF_2$ at w|IL interface. Potentials were referenced to the effective point-of-zero-charge (E_{pzc}) taken to be the midpoint between the positive and negative limits of the polarizable potential window (PPW). The black dashed-lined curve illustrates the experimental response with no $LiBH_4$ added to the IL phase. The PPW for $P_{66614}NTf_2$ is ~400 mV wide in good agreement with results from previous research.[14] Stockmann *et al.*[15] showed that the PPW is limited by transferring NTf_2^- from IL to water at positive potentials and SO_4^{2-} from water to IL at negative potentials. While P_{66614}^+ and Li^+ can transfer as well, they are likely small contributors to the current limiting the PPW since, as is mentioned above, P_{66614}^+ is quite hydrophobic and Li^+ has a higher formal ion transfer potential ($\Delta_{\mathrm{IL}}^{\mathrm{w}}\phi_{Li^+}^{\mathrm{o}}$)[10, 16] than NTf_2^-. After adding the $LiBH_4$ to the IL, a BH_4^- onset transfer wave appeared at roughly –0.12 V.

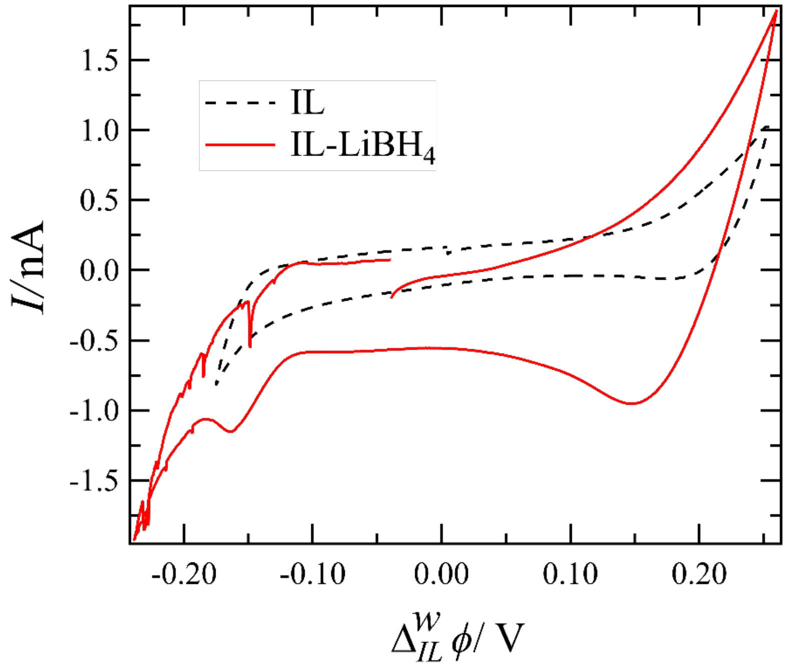

Figure 3.1: Cyclic voltammetry at a micro w|IL interface with 1.2 M $LiBH_4$ dissolved in IL using Cell 1. The red trace is after adding the $LiBH_4$ and the black one is only IL. Scan rate of 0.020 V s^{-1}

To investigate further, CA at the w|$P_{66614}NTf_2$ interface was recorded at –0.2 V (*vs*. PZC) with and without $LiBH_4$ added, Figures 3.2A and B, respectively. Without $LiBH_4$ added, the *i-t* curves elicited the typical chronoamperometric response with limited background noise of roughly 0.43 pA; however, after adding 1.2 M $LiBH_4$ negative spikes were observed. Since inorganic salts have low solubility in ILs with which they do not share a common ion,[17] these negative current spikes are likely associated with $LiBH_4$ nanocrystal (NC) stochastic impacts. Indeed, this agrees well with a recent report by Stockmann *et al.*[15], who proposed a non-faradaic, capacitive mechanism for

$LiBH_4$ NC impact events at w|IL micro-interfaces. The negative charge is adsorbed at the interface in this mechanism causing negative current spikes.

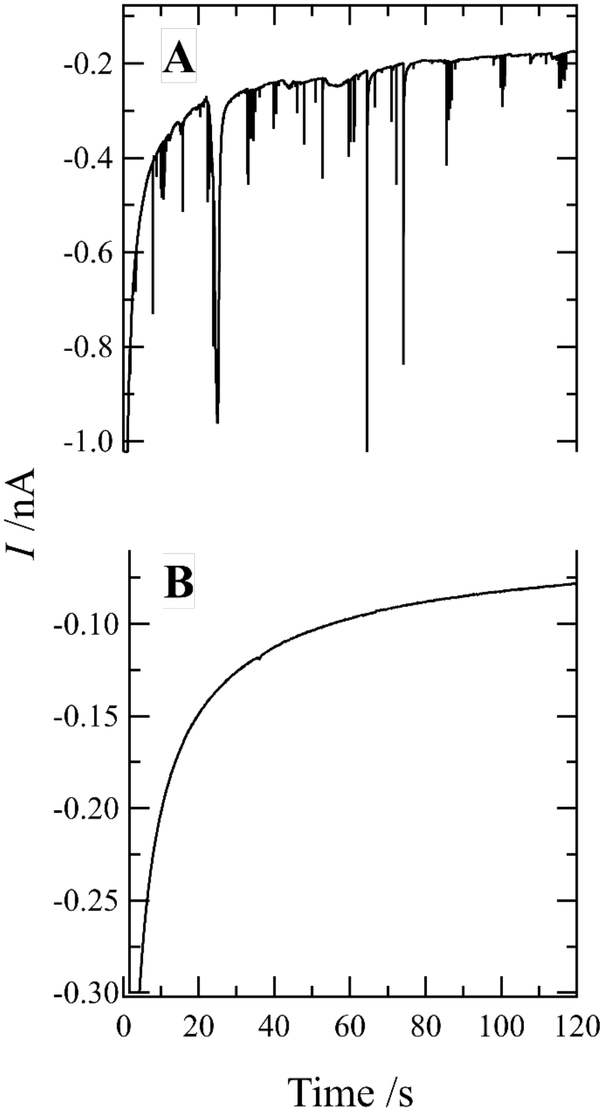

Figure 3.2: Chronoamperograms (CA) recorded at a 25 μm diameter w|$P_{66614}NTf_2$ interface with (**A**) and without (**B**) 1.2 M $LiBH_4$ dissolved in the $P_{66614}NTf_2$ phase. The potential step pulse was applied from 0.0 to –0.2 V.

Next, the influence of Pt NPs was investigated by CA using two different concentrations of Pt NPs in $P_{66614}NTf_2$ in which two different concentrations of $LiBH_4$ were also employed in the synthesis of the Pt NP (see Figure 3.3). After adding the Pt NPs, a small number of positive current peaks were observed. It was hypothesized that these spikes were owing to Pt NP stochastic impacts at the w|IL interface. The number of positive current spikes increased concomitantly with increasing Pt NP concentration and decreasing the $LiBH_4$ concentration.

The average positive peak current intensity at 3.22×10^{16} Pt NP cm^{-3} was 4.04 pA, and by increasing the NPs concentration, the average peak intensity increased to 10.9 pA. This enhancement in intensity may be due to the size of the Pt NPs. Using a smaller amount of $LiBH_4$ in the synthesis of the Pt NPs, resulted in bigger NPs. However, at the same time, as [$LiBH_4$] decreased, the intensity of the negative peak currents decreased from –84.2 pA to –23.3 pA. Therefore, we could say that the positive current spikes could be the Pt NPs impact at the w|IL. It is unclear however, if these current spikes are Pt NP electrocatalysis of the BOR.

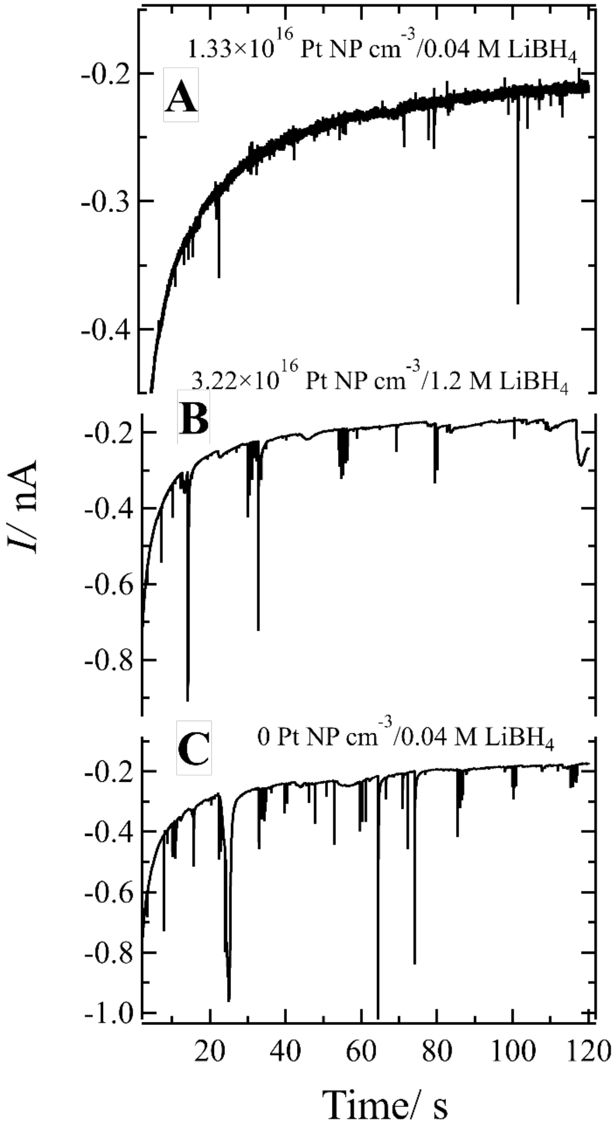

Figure 3.3: CAs performed at *E* = –0.2 V using cell 1 with [Pt NP]/[$LiBH_4$] equal to 1.33×10^{16} Pt NP cm^{-3}/0.04 M (**A**) **B** 3.22×10^{16} Pt NP cm^{-3}/1.2 M (**B**) and 0/1.2 M (**C**). All other experimental parameters were the same as described in Figure 3.2.

Thus, to eliminate interference from $LiBH_4$ NCs and excess solubilized $LiBH_4$, IL/Pt NP/$LiBH_4$ solutions were treated with acetone which was subsequently removed with heating at ~60°C under high vacuum. Since $LiBH_4$ is a strong reducing agent, it should be converted to less reactive boric acid or lithium metaborate after reaction with acetone. The CA recorded after acetone treatment (Figure 3.4A) showed a marked decrease in current spikes compared to before treatment (Figure 3.4B). The TEM images from after acetone treatment on Pt NPs are shown in Figure B1 in Appendix B.

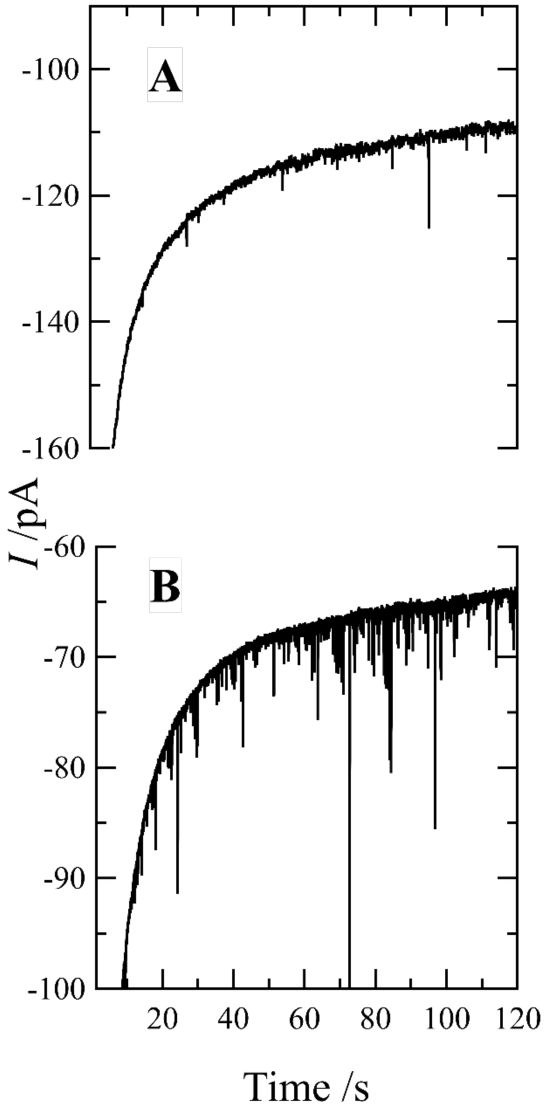

Figure 3.4: *i-t* Curves measured after (A) and before (B) treatment with 200 μL of acetone to a 1 mL IL solution. All other experimental conditions were the same as description in Figure 3.2B.

After oxidation of $LiBH_4$ with acetone, methanol was added iteratively to 3.22×10^{16} Pt NP cm^{-3} in $P_{66614}NTf_2$ solution with *i-t* responses measured between each addition. CAs were recorded at both CF UME and micro w|IL interface. Figure 3.5A and B depict the *i-t* response measured at $E = 1.7$ V (*vs*. QRE) at a 7 μm diameter CF UME after and before adding 40 μL of CH_3OH to the NP/IL solution. After CH_3OH addition, positive spikes appeared, which are likely owing to Pt NP ECA of CH_3OH oxidation. These spikes could be due to single NP impact events. However, because CH_3OH probably disrupts the supramolecular fluidic nature of the IL phase, which is responsible for NP stability and prevents NP aggregation, these spikes are more likely NP aggregates or clusters of NPs impacting the UME surface. The mechanism of NP aggregation in a bulk IL phase is still unclear and this investigation is on-going in our lab.

Nevertheless, these results agree well with previous reports[18] of Pt NP electrocatalytic behaviour towards the CH_3OH oxidation reaction. Figure B2 in Appendix B shows a CV performed in a similar mixture with 40 μL CH_3OH added to $P_{66614}NTF_2$, however, at a 25 μm diameter Pt UME. This CV closely resembles the *i-V* response at a macro-electrode.[19-20] In Figure B2, the CV started from 0 V and moved toward positive potentials. Because the Pt UME surface is contaminated by carbon monoxide, oxidation of CH_3OH is not observed in the forward scan. By moving toward high positive potential all CO completely is oxidized. Therefore, in the reverse scan the Pt surface was free to catalyze methanol oxidation and an anodic peak was observed in the backward scan.

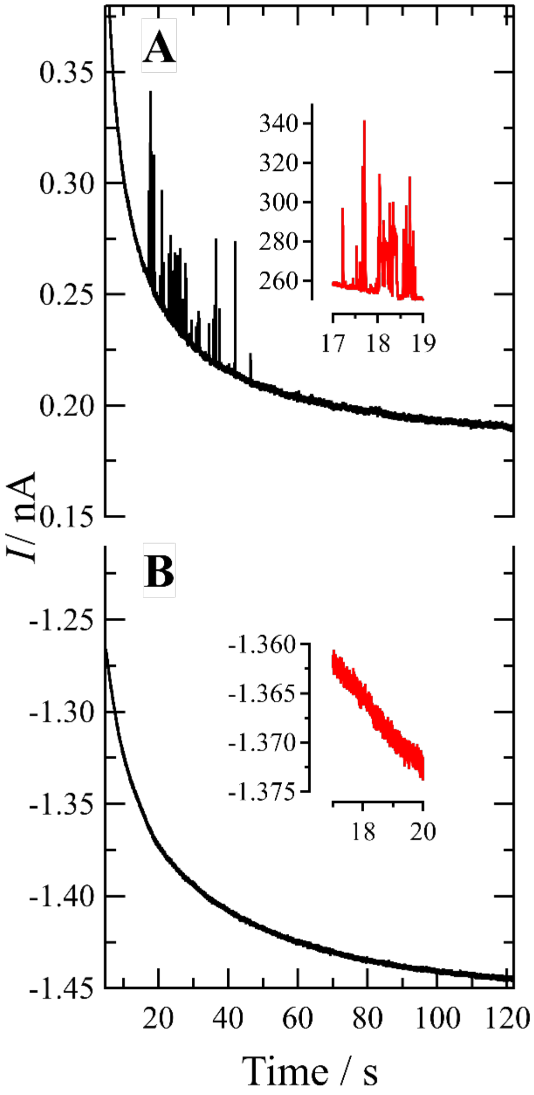

Figure 3.5: CAs performed at E = 1.7 V (*vs*. QRE) using a 7 µm diameter CF UME with [Pt NP] = 3.22×10^{16} NP cm^{-3}, after (**A**) and before (**B**) addition of 40 µL of CH_3OH methanol.

A similar experiment was performed using Cell 1 at the w|IL micro-interface with the Pt NP-IL solution and after adding the 10 and 40 µL CH_3OH (Figure 3.6). Before adding methanol, there were a few tiny positive current spikes, but by adding 10 µL of CH_3OH, large positive peak currents were observed. By increasing the amount of methanol, the current intensity increased from 0.36 to 0.78 nA. We propose that in this case, methanol was oxidized in the IL and donated the electrons through Pt NPs to water, and in water, oxygen reduction reaction (ORR) accepts electrons. Thus, the positive current may be due to charge transfer from IL to water across the Pt NPs adsorbed at the LLI. In addition, the current enhancement in w|IL could be due to a reduction in the overall viscosity of IL.

In Figure 3.7, the proposed mechanism for electrocatalytic methanol oxidation reaction by Pt NPs at both CF UME and w|IL interface is drawn.

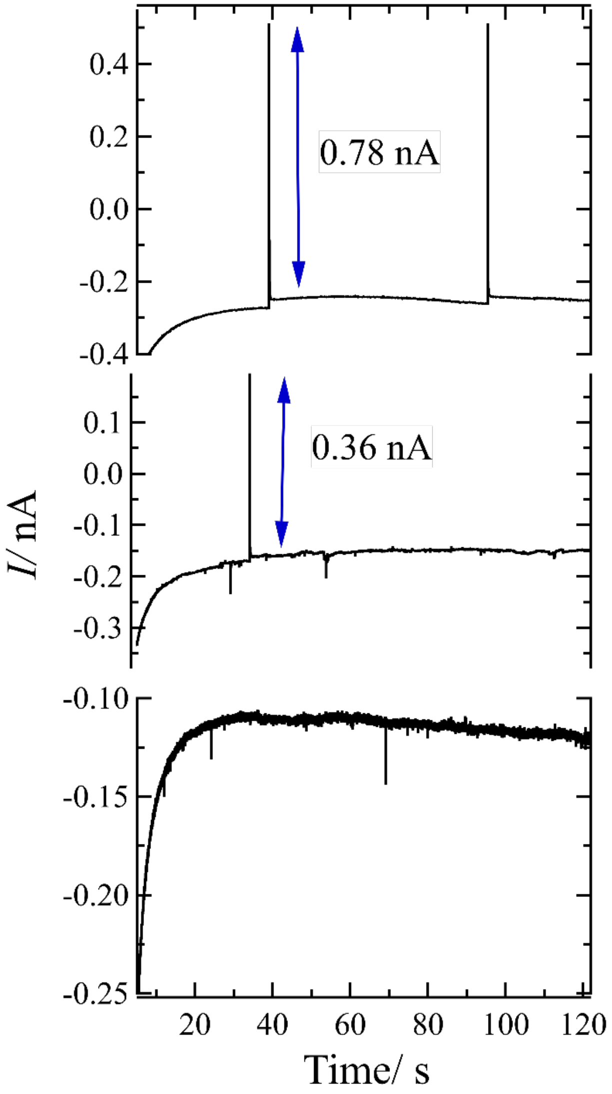

Figure 3.6: Chronoamperogram (CA) recorded using 3.22×10^{16} Pt NP cm^{-3} in IL at w|IL (Cell 1) with (**A**) 40, (**B**) 10, and (**C**) without 0 µL methanol at $E = -0.2$ V (*vs.* PZC).

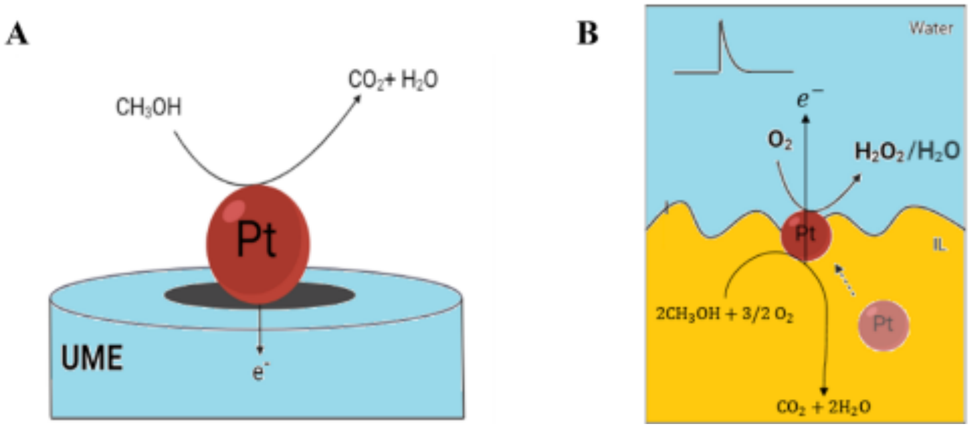

Figure 3.7: Scheme of Pt NP mediated electrocatalytic amplification mechanisms of CH_3OH oxidation at a UME (**A**) and w|IL interface (**B**).

Similarly, the influence of ferrocene (Fc) as an electron donor was investigated by adding 10 mM Fc to the Pt-IL solution(Cell 1). First, the system in the absence of Pt and $LiBH_4$ was studied by recording the CA for 10 mM Fc dissolved in $P_{66614}NTF_2$ at w|IL interface (Figure 3.8C). An utterly smooth curve without any current spikes was observed. After adding 1.2 M $LiBH_4$ to the previous solution, only negative current transients, according to BH_4^- impacts, appeared. The exciting result was achieved by adding the 10 mM Fc to the Pt-IL solution. A huge enhancement in both negative and positive current transient frequency was observed (Figure 3.8A). Two different mechanisms were hypothesized. In the first mechanism (Figure 3.9A), Fc stays in the IL phase and is oxidized to ferrocenium at the Pt NPs surfaces. The electron transfers from IL to water across the Pt NPs and ORR is electrocatalyzed in the water phase through this pathway. As a result, the frequency of positive currents spikes increased. In the second mechanism (Figure 3.9B), Fc partitions into the water phase and the reverse occurs with ORR taking place in the IL phase. Thus, electrons are donated from water to IL across the Pt NP. Since there is some O_2 in the IL, the ORR can occur in the IL phase. This mechanism could explain the increasing number of negative current spikes.

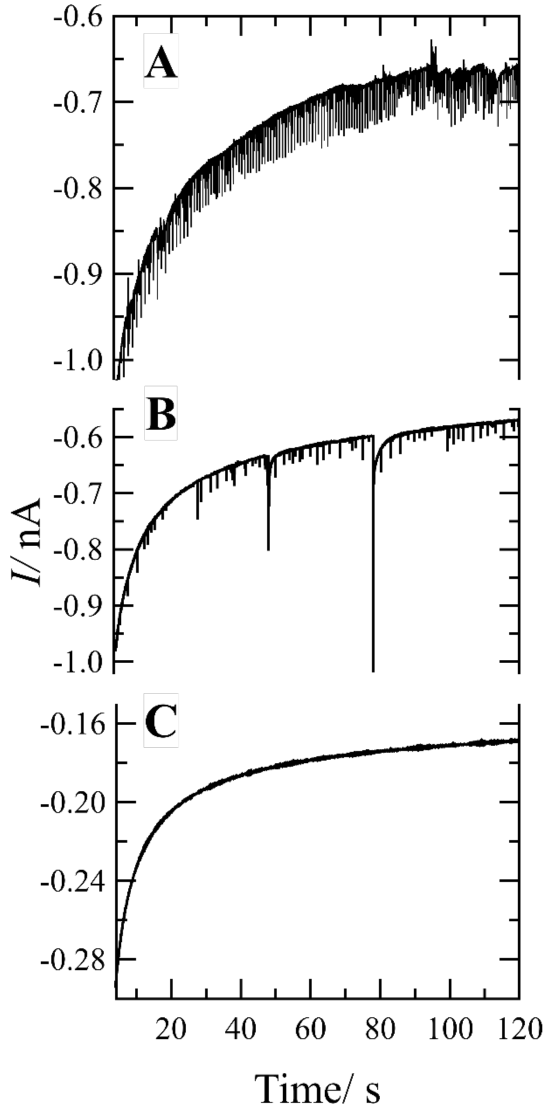

Figure 3.8: Chronoamperograms (CA) measured at w|IL interface with 10 mM of Fc in the IL phase and (**A**) in the presence of Pt NPs and (**B**) absence of Pt NPs, both with 1.2 M $LiBH_4$ dissolved in IL; (**C**) only IL and 10 mM Fc.

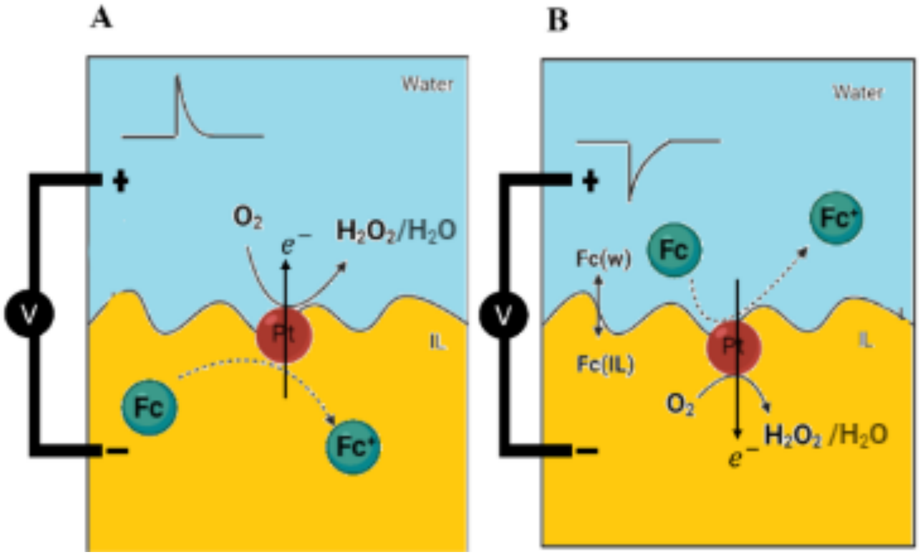

Figure 3.9: Cartoons of two different proposed mechanisms at w|IL interface of Pt-IL solution in presence of Fc.

3.5. Conclusion

Herein, Pt NPs were investigated at a w|IL interface by the electrocatalytic amplification method. The Pt NPs were shown to act as electrocatalysts for both $LiBH_4$ and methanol oxidation reactions via detection through the electrocatalytically enhanced charge transfer reactions mediated by the NPs at the w|IL micro-interface.

Through these data, Pt NPs were proposed to act as electrocatalysts through a number of different mechanisms for both ORR and BOR. These results are in agreement with previous results that are mentioned in Chapter 2 and also with that of Watanabe *et al.*,[21] who studied the catalytic activity of platinum for methanol oxidation mechanism for methanol fuel cell applications in 1989.

Also, the enhancement in the current peak after adding methanol provided evidence that adding a polar solvent to the IL helps to destroy the supramolecular fluidic nature of the IL and resulted in the likely formation of NP agglomerates.[22]

3.6. References

1. Xiao, X.; Fan, F.-R. F.; Zhou, J.; Bard, A. J., Current Transients in Single Nanoparticle Collision Events. *J. Am. Chem. Soc***. 2008,** *130* (49), 16669-16677.

2. Haddou, B.; Rees, N. V.; Compton, R. G., Nanoparticle–electrode Impacts: The Oxidation of Copper Nanoparticles Has Slow Kinetics. *Phys. Chem. Chem. Phys.* **2012,** *14* (39), 13612-13617.

3. Lim, C. S.; Tan, S. M.; Sofer, Z.; Pumera, M., Impact Electrochemistry of Layered Transition Metal Dichalcogenides. *ACS Nano* **2015,** *9* (8), 8474-8483.

4. Gooding, J. J., Single Entity Electrochemistry Progresses to Cell Counting. *Angew. Chem. Int. Ed.* **2016,** *55* (42), 12956-12958.

5. Oja, S. M.; Robinson, D. A.; Vitti, N. J.; Edwards, M. A.; Liu, Y.; White, H. S.; Zhang, B., Observation of Multipeak Collision Behavior During The Electro-oxidation of Single Ag Nanoparticles. *J. Am. Chem. Soc* **2017,** *139* (2), 708-718.

6. Colombi Ciacchi, L.; Köppen, S., Nanoscale Properties of Solid–Liquid Interfaces. In *Encyclopedia of Nanotechnology*, Bhushan, B., Ed. Springer Netherlands: Dordrecht, 2012; pp 1728-1733.

7. Gründer, Y.; Fabian, M. D.; Booth, S. G.; Plana, D.; Fermín, D. J.; Hill, P. I.; Dryfe, R. A., Solids at The Liquid–liquid Interface: Electrocatalysis with Pre-formed Nanoparticles. *Electrochim. Acta* **2013,** *110*, 809-815.

8. Scanlon, M. D.; Smirnov, E.; Stockmann, T. J.; Peljo, P., Gold Nanofilms at Liquid–liquid Interfaces: an Emerging Platform for Redox Electrocatalysis, Nanoplasmonic Sensors, and Electrovariable Optics. *Chem. Rev.* **2018,** *118* (7), 3722-3751.

9. Stockmann, T. J.; Angele, L.; Brasiliense, V.; Combellas, C.; Kanoufi, F., Platinum Nanoparticle Impacts at a Liquid| liquid Interface. *Angew. Chem. Int.* **2017,** *129* (43), 13678-13682.

10. Stockmann, T. J.; Guterman, R.; Ragogna, P. J.; Ding, Z., Trends in Hydrophilicity/lipophilicity of Phosphonium Ionic Liquids as Determined by Ion-transfer Electrochemistry. *Langmuir* **2016,** *32* (49), 12966-12974.

11. Girault, H., Electrochemistry of Liquid-liquid Interfaces. *" Electroanalytical Chemistry"* **1989,** *15*, 1.

12. Bard, A. J.; Faulkner, L. R., Fundamentals and Applications. *Electrochem. Methods* **2001,** *2* (482), 580-632.

13. Sanchez Vallejo, L.; Ovejero, J.; Fernández, R.; Dassie, S., Simple Ion Transfer at Liquid| liquid Interfaces. *Int. J. Electrochem.* **2012**.

14. Tsujioka, N.; Imakura, S.; Nishi, N.; Kakiuchi, T., Voltammetry of Ion Transfer Across The Electrochemically Polarized Micro Liquid-liquid Interface Between Water and a Room-

temperature Ionic Liquid, Tetrahexylammonium Bis(trifluoromethylsulfonyl)imide, Using a Glass Capillary Micropipette. *Anal Sci* . **2006,** *22* (5), 667-671.

15. Stockmann, T. J.; Lemineur, J.-F.; Liu, H.; Cometto, C.; Robert, M.; Combellas, C.; Kanoufi, F., Single $LiBH_4$ Nanocrystal Stochastic Impacts at A Micro Water| ionic Liquid Interface. *Electrochim. Acta* **2019,** *299*, 222-230.

16. Stockmann, T. J.; Ding, Z., Tetraoctylphosphonium Tetrakis(pentafluorophenyl)borate Room Temperature Ionic Liquid Toward Enhanced Physicochemical Properties for Electrochemistry. *J. Phys. Chem. B* **2012,** *116* (42), 12826-12834.

17. Pereiro, A.; Araújo, J.; Oliveira, F.; Esperança, J.; Lopes, J. C.; Marrucho, I.; Rebelo, L., Solubility of Inorganic Salts in Pure Ionic Liquids. *J. Chem. Thermodyn.* **2012,** *55*, 29-36.

18. Moghaddam, R. B.; Pickup, P. G., Support Effects on The Oxidation of Methanol at Platinum Nanoparticles. *Electrochem. Commun.* **2011,** *13* (7), 704-706.

19. Narayanamoorthy, B.; Datta, K. K. R.; Eswaramoorthy, M.; Balaji, S., Highly Active and Stable Pt_3 Rh Nanoclusters as Supportless Electrocatalyst for Methanol Oxidation in Direct Methanol Fuel Cells. *ACS Catalysis* **2014,** *4* (10), 3621-3629.

20. Fu, Z.; Li, W.; Zhang, W.; Sun, F.; Zhou, Z.; Xiang, X., Preparation and Activity of Carbon-supported Porous Platinum as Electrocatalyst for Methanol Oxidation. *Int. J. Hydrog. Energy* **2010,** *35* (15), 8101-8105.

21. Watanabe, M.; Saegusa, S.; Stonehart, P., High Platinum Electrocatalyst Utilizations for Direct Methanol Oxidation. *J. Electroanal. Chem. Interf. Electrochem.* **1989,** *271* (1-2), 213-220.

22. Robinson, D. A.; Kondajji, A. M.; Castañeda, A. D.; Dasari, R.; Crooks, R. M.; Stevenson, K. J., Addressing Colloidal Stability for Unambiguous Electroanalysis of Single Nanoparticle Impacts. *J. Phys. Chem. Lett.* **2016,** *7* (13), 2512-2517.

Chapter 4

4.1. Conclusions and Perspectives

Initial investigations explored NP translocation by the resistive pulse method within an IL. There have been many previous reports into resistive pulse experiments studying NP translocation using a solid-state nanopore;[1-5] however, none focusing on these events occurring within a pure IL phase. Our initial research program began looking into first, how the viscosity, high ionic strength, and supramolecular fluidic nature of the IL phase would impact NP translocation. Few studies have employed ILs to investigate NP translocation because of their high viscosity. However, this aspect of the IL can be exploited to decrease the speed at which a NP or biomolecule (*e.g.*, DNA) translocates enhancing measurement resolution.[6] Indeed, a major bottleneck towards using resistive pulse technology towards DNA sequencing is that DNA transits the pore too quickly to be resolved by present-day instrumentation. ILs have also been shown to help stabilize the DNA molecule against degradation for long-term storage. Thus, an innovative solution to both reduce the speed at which the DNA translocates and improve its storage capabilities, was to employ an IL.

Using a glass nanopipette as a solid-state nanopore is a standard method in the resistive pulse technique. The nanopipette is composed of a glass or quartz pipette with a pore radius between 1 and 100 nm. Nanopipettes have found many applications in analytical chemistry, nanoelectrochemistry, bionanotechnology, and biosensing according to its size, geometry, and surface chemistry.[7] Nanopipettes were prepared following a method developed by Silver *et al.*[8-9]

Preliminary results using TiO_2 NPs generously provided by the Katz group at Memorial University were promising. In this experiment, 20 mg of TiO_2 NPs were dispersed in 1 mL $P_{66614}NTf_2$ and installed inside a nanopipette with pure $P_{66614}NTf_2$ outside. The CA curve depicted in Figure 4.1 was recorded over 6 hours. Each positive spike is associated with the translocation of one or multiple NPs through the pore.

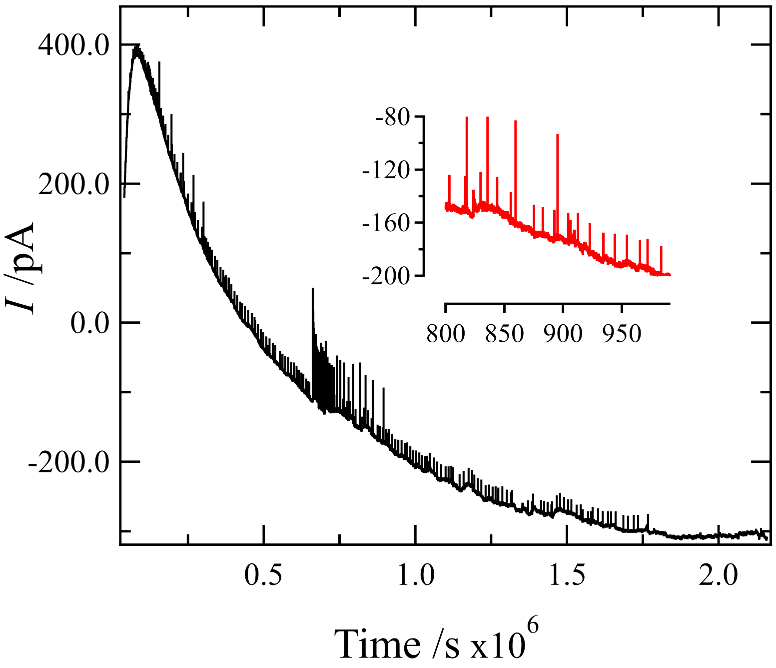

Figure 4.1: CA curve recorded over 6 hours using a $P_{66614}NTf_2$ solution containing 20 mg TiO_2 NPs per 1 mL $P_{66614}NTF_2$ loaded into a nanopipette which was positioned inside a second $P_{66614}NTf_2$ solution without TiO_2 NPs added.

The flux of NPs in the nanopipette was calculated through equation 4.1,[10]

$$f = \frac{D_{Np} c_{Np} \pi r_a^2}{r_a + L} \qquad 4.1$$

Where D_{Np} and c_{Np} are diffusion coefficient and concentration of NPs, while r_a and L are the radius and height of the nanochannel, respectively.

During this research, some technical problems arose. First, calculating the concentration of TiO_2 was challenging since Dr. Katz has reason to believe that they are hollow, making their density and shell thickness an open question. Also, consistent nanopipette fabrication proved difficult. A more affective fabrication method involves the use of a laser pipette puller which was not available due to COVID-19 restrictions. In addition, the high background noise (~8.7 pA) was another issue.

In light of these problems, the research program switched to using SEE through stochastic impacts similar to that described by Xiao *et al.*[11] in 2007. Pt and Au NPs were prepared using $LiBH_4$ as a reducing agent and $P_{66614}NTF_2$ as the reaction solvent medium. This results in small (<20 nm diameter) and monodisperse NPs. The Pt NPs could be detected by acting as an electrocatalyst for BOR at a CF UME. By recording the CV from $LiBH_4$-IL solution at Pt UME, the activity of Pt was investigated directly. It was found that the BOR is sluggish at a CF UME, but it electrocatalyzed at a Pt surface, in agreement with previous reports. [11-13] By adding the Fc to the solution and performing CV in the same solution at CF UME, it was discovered that BH_4^-, dissolved in the IL phase, re-reduced any Fc^+ electrogenerated at the electrode surface through an EC′ mechanism. These data also suggest that $LiBH_4$ is relatively insoluble in the IL phase and forms NCs once any organic solvent is removed and is in agreement with a recent report by Stockmann *et al.*[13] Pt NPs suspended in an IL was also investigated. By recording the CA in a Pt NP/IL solution, Pt NP stochastic impacts at a CF UME increased by Pt NPs acting as an electrocatalyst for the BOR. The same experiment was performed using Au NPs; however, these experiments did not show any catalytic behavior of Au NP towards BOR, which was in good agreement with previous studies. For example, Mirkin *et al.*,[14] who studied the mechanism of the BOR at an inlaid disc Au UME, which did not act as BOR electrocatalyst and was ostensibly chosen for that reason. The critical physical insight gained through these experiments was that small additions of polar molecular solvents disrupted the supramolecular nature of the IL phase, promoting NP aggregation.

Next, in Chapter 3, preliminary tests were performed investigating Pt NP stochastic impacts, this time at a LLI between w|IL. Stockmann *et al.*[10] in 2017 published work on Pt NP impacts at w|DCE interface in the presence of Fc as an electron donor. As mentioned in Chapter 1, the ILs are known as highly stable electrolytes[15] and solvents for synthesis of metal NPs.[16] In Chapter 3, those two properties of ILs were exploited to study Pt NPs electrocatalytic behavior at a w|IL interface for the BOR and methanol oxidation reaction. Pt NPs were detected by electrocatalytic amplification of these reactions in which electron were transferred from w→IL or IL→w with the NP acting as a catalyst cite and electron transfer mediator at the w|IL interface. The $LiBH_4$-IL solution with and without Pt was investigated at w|$P_{66614}NTf_2$. We found that by increasing the concentration of Pt, the positive current spikes increased. This was explained by Pt NP electrocatalyzed BOR electron transferred across the Pt to the aqueous phase to simultaneously reduce dissolved O_2. However, these are preliminary results, and the mechanism is still under investigation.

Next, excess $LiBH_4$ added to the IL phase to generate the NPs was oxidized by treatment with acetone in order to reduce its reactivity and transform BH_4^- to less reactive boric acid or other oxidized species. In this way, Pt NPs could be interrogated towards methanol oxidation. Indeed, similar to the BOR, Pt NPs electrocatalyzed the methanol oxidation reaction, and Pt NPs were detected based on electrons transferring from IL→w across the NP. Then, Fc as an electron donor in Pt NP/IL solution was studied. By adding Fc to the system, the observable frequency of both $LiBH_4$ NC and Pt NP impacts increased. Moreover, both positive and negative current spikes were observed, both at enhanced frequencies. To describe this system, it was proposed that Fc partitions across the interface, while some remains in the IL phase; thus, it is capable of donating electrons across the LLI using the Pt NP as an electrocatalytic mediator in either direction, w→IL (negative spike) or IL→w (positive spike).

Subsequent research programs will try to elucidate these mechanisms further using Fc-functionalized phosphonium ILs synthesized in-house through a synthetic method reported by Weaver *et al.*;[17] see Figure 4.2. In this way, electron transfer and mass transport of four different redox active Fc functionalized alkylphosphonium ILs will be investigated simply by increasing the alkyl chain length on the Fc-modified arm attached to the phosphonium core. By increasing *n* (see Figure 4.2), one expects that molecule **1** will be amphiphilic such that the Fc group will be able to partition into the aqueous phase while the hydrophobic phosphonium-part will remain in the IL phase. As a result, the Fc moiety will donate the electron from water to IL, and negative current spikes would be expected (Figure 4.3).

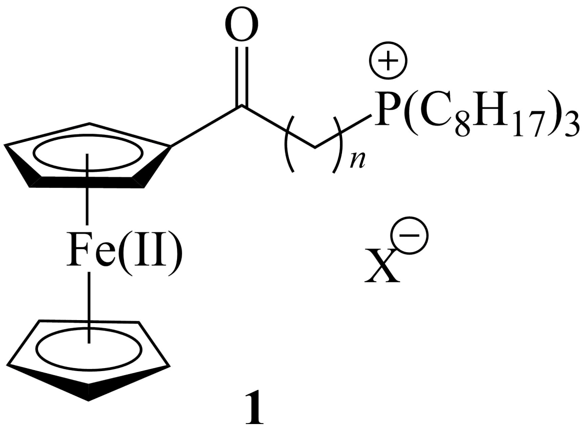

1

Figure 4.2: The structure of Fc-functionalized phosphonium IL with different acyl chain lengths (n), where X^- is the counter anion which could be Br^-, NTf_2^-, or $B(C_6F_5)_4^-$.

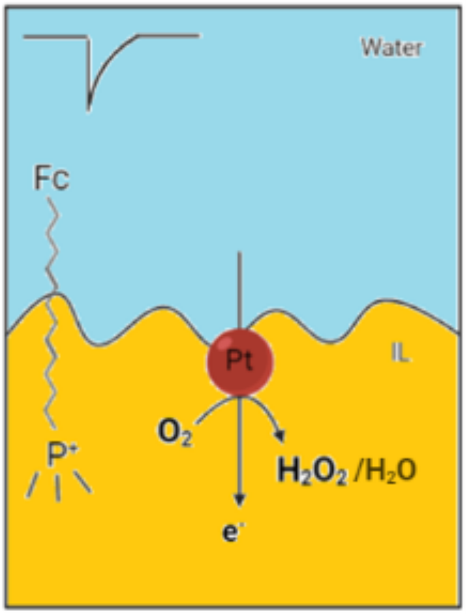

Figure 4.3: Mechanism of Fc modified phosphonium IL partition at LLI for studying Pt NP stochastic impacts.

4.2. References

1. German, S. R.; Hurd, T. S.; White, H. S.; Mega, T. L., Sizing Individual Au Nanoparticles in Solution with Sub-nanometer Resolution. *ACS nano* **2015,** *9* (7), 7186-7194.

2. McKelvey, K.; Edwards, M. A.; White, H. S., Resistive Pulse Delivery of Single Nanoparticles to Electrochemical Interfaces. *J. Phys. Chem. Lett.* **2016,** *7* (19), 3920-3924.

3. Zhang, Y.; Edwards, M. A.; German, S. R.; White, H. S., Multipass Resistive-pulse Observations of the Rotational Tumbling of Individual Nanorods. *J. Phys. Chem. C* **2016,** *120* (37), 20781-20788.

4. Wang, Y.; Wang, D.; Mirkin, M. V., Resistive-Pulse and Rectification Sensing with Glass and Carbon Nanopipettes *Proc. R. Soc. A: Mathematical, Physical and Engineering Sciences* **2017,** *473* (2199), 20160931.

5. Yu, Y.; Sundaresan, V.; Bandyopadhyay, S.; Zhang, Y.; Edwards, M. A.; McKelvey, K.; White, H. S.; Willets, K. A., Three-dimensional Super-resolution Imaging of Single Nanoparticles Delivered by Pipettes. *ACS Nano* **2017,** *11* (10), 10529-10538.

6. Carson, S.; Wanunu, M., Challenges in DNA Motion Control and Sequence Readout Using Nanopore Devices. *Nanotechnology* **2015,** *26* (7), 074004.

7. Chen, Q.; Liu, Z., Fabrication and Applications of Solid-state Nanopores. *Sensors* **2019,** *19* (8), 1886.

8. Silver, B. R.; Holub, K.; Mareček, V., A Simple Electrochemical Methodology for Evaluation of The Velocity of Electroosmotic Flow at The Tip of Polarized Microcapillary. *Electrochim. Acta* **2015,** *156*, 316-320.

9. Silver, B.; Holub, K.; Mareček, V., Low Frequency Pseudo-inductive Phenomenon at Novel Glass Microcapillaries Exhibiting Non-ohmic Behaviour. *Electrocim. Acta* **2013,** *110*, 801-808.

10. Stockmann, T. J.; Angele, L.; Brasiliense, V.; Combellas, C.; Kanoufi, F., Platinum Nanoparticle Impacts at A Liquid| liquid Interface. *Angew. Chem. Int. Ed* **2017,** *129* (43), 13678-13682.

11. Xiao, X.; Bard, A. J., Observing Single Nanoparticle Collisions at An Ultramicroelectrode by Electrocatalytic Amplification. *J. Am. Chem. Soc* **2007,** *129* (31), 9610-9612.

12. Martins, J.; Nunes, M.; Koch, R.; Martins, L.; Bazzaoui, M., Electrochemical Oxidation of Borohydride on Platinum Electrodes: The Influence of Thiourea in Direct Fuel Cells. *Electrochim. acta* **2007,** *52* (23), 6443-6449.

13. Stockmann, T. J.; Lemineur, J.-F.; Liu, H.; Cometto, C.; Robert, M.; Combellas, C.; Kanoufi, F., Single $LiBH_4$ Nanocrystal Stochastic Impacts at A Micro Water| ionic Liquid Interface. *Electrochim. Acta* **2019,** *299*, 222-230.

14. Mirkin, M. V.; Yang, H.; Bard, A. J., Borohydride Oxidation at A Gold Electrode. *J. Electrochem. Soc* **1992,** *139* (8), 2212.

15. Jonsson, E., Ionic Liquids as Electrolytes for Energy Storage Applications–A Modelling Perspective *Energy Storage Mater.* **2020,** *25*, 827-835.

16. Richter, K.; Campbell, P. S.; Baecker, T.; Schimitzek, A.; Yaprak, D.; Mudring, A. V., Ionic Liquids for The Synthesis of Metal Nanoparticles. *Phys. Status Solidi B* **2013,** *250* (6), 1152-1164.

17. Weaver, J. E.; Breadner, D.; Deng, F.; Ramjee, B.; Ragogna, P. J.; Murray, R. W., Electrochemistry of Ferrocene-functionalized Phosphonium Ionic Liquids. *J. Phys. Chem. C* **2011,** *115* (39), 19379-19385.

Appendix A

A. Supporting Information for Chapter 2

A.1. Root Mean Square Calculation

The root mean square (rms) of the noise was calculated form a 1 second segment of the noise from the blank curve from 69 to 70 s, see Figure 2.4A in the main text, which included $N = 5001$ data points using the following equation,

$$rms = \sqrt{\frac{\sum_{i=1}^{N}\left(x_i - \overline{x}_i\right)^2}{N}} \qquad [A1]$$

In which $\overline{x}_i$ is the mean signal value.

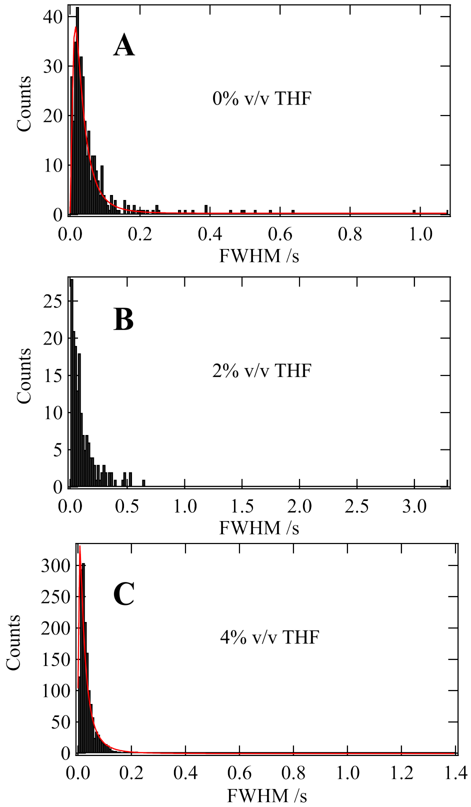

Figure A1: Histograms from Pt NP impact analysis of *i*-*t* curves for $c_{\mathrm{NP}} = 3.66\times10^{16}$ NP cm^{-3} in $P_{66614}NTf_2$ containing $[LiBH_4]_{eff} = 1.2$ M and after addition of 0, 2%, and 4% v/v THF for panels A, B, and C, respectively. CA curves are shown in Figures 2.7A, 2.9A, and 2.9B, respectively, in the main text.

A.2. TEM Image of Gold NPs

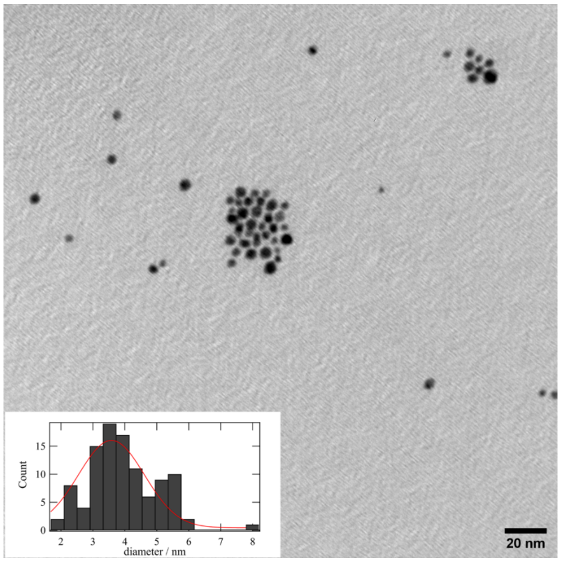

Figure A2:TEM image of gold NPs. Inset is a histogram of the particle size distribution.

A.3. Cyclic Voltammetric Response of 1.2 M $LiBH_4$ in IL after Adding Acetone at Carbon UME

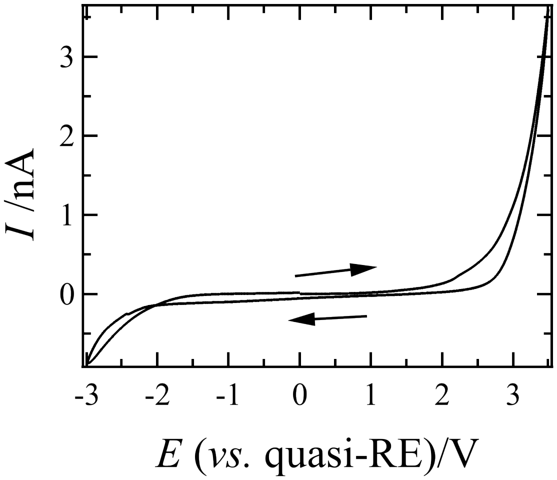

Figure A3: CV recorded with a CF UME in 1.2 M $LiBH_4$ in $P_{66614}NTf_2$ after washing with ~500 μL of acetone for 10 min with stirring, which was subsequently removed under vacuum with heating at 60°C. A scan rate of 0.050 V s^{-1} was used.

Appendix B

B. Supporting Information for Chapter 3

B.1. TEM Image of Pt NPs in the Presence of Acetone

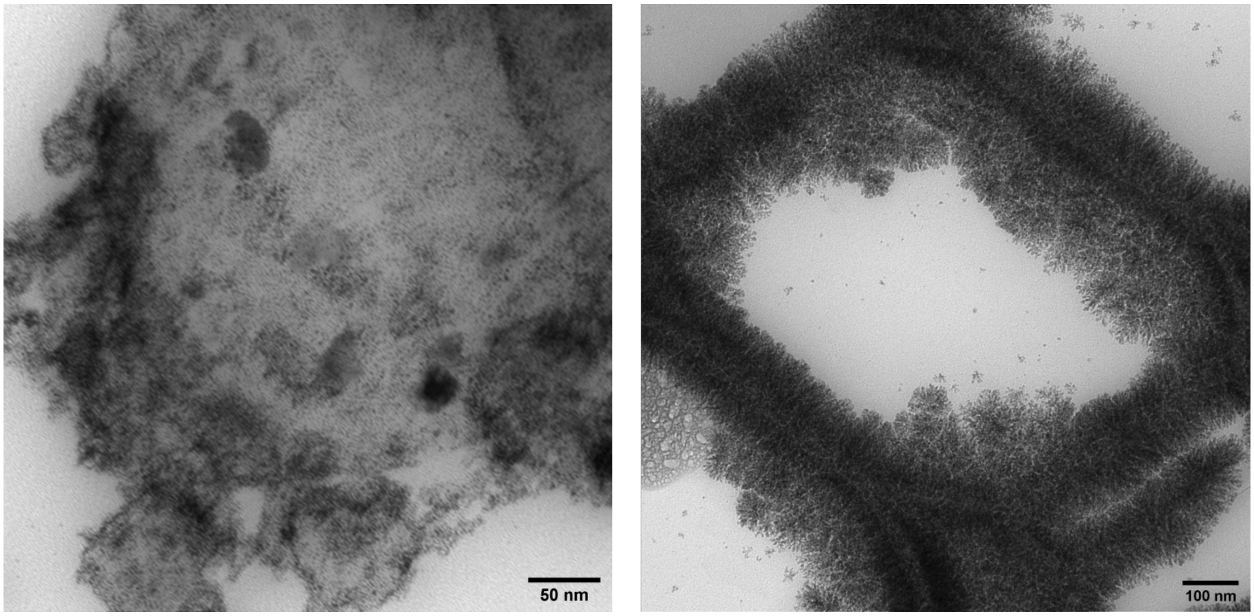

Figure B1: TEM imaging from adding 200 μL acetone to Pt-IL solution

B.2. Cyclic Voltammetric Response of Methanol Oxidation at Pt UME

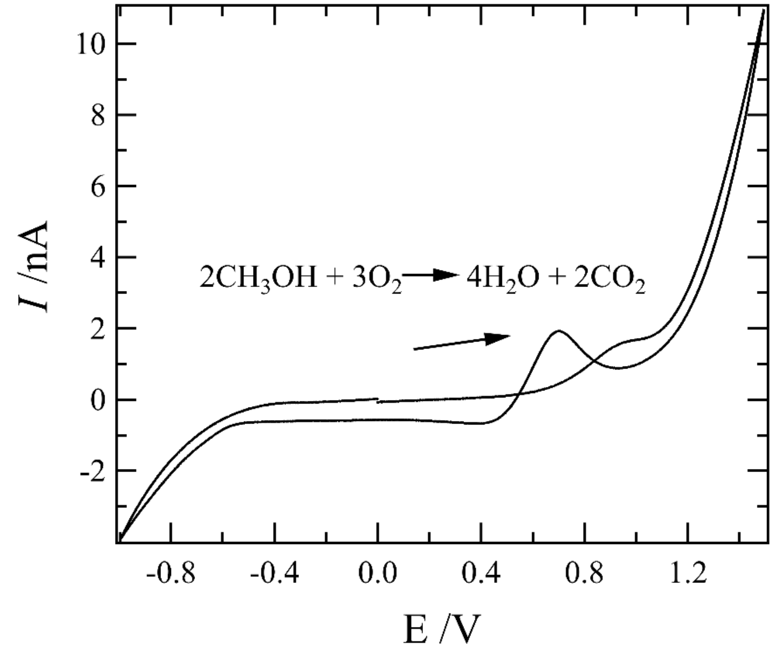

Figure B2: Cyclic voltammetric of 10 µL methanol in $P_{66614}NTF_2$ at Pt UME.

Appendix C

C. Supporting Information for Chapter 4

C.1. TEM image of TiO_2 Particles

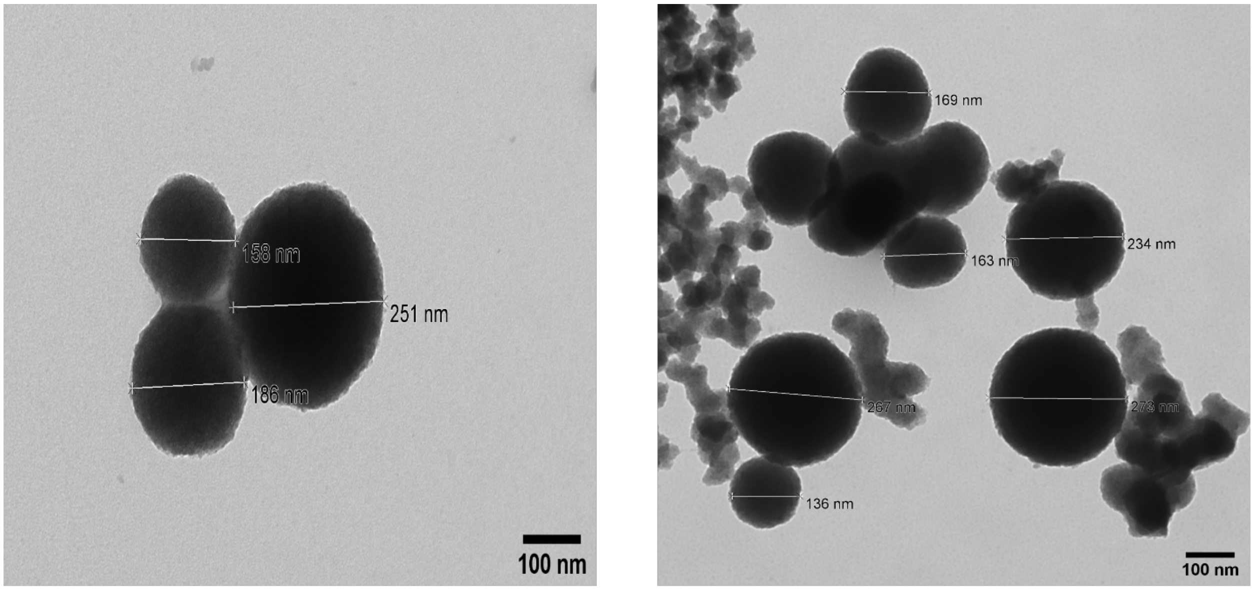

Figure C1: Size of TiO_2 NPs with TEM imaging.